Lateral variations of detrital, authigenic and petrophysical properties in an outcrop analog of the fluvial Plattensandstein, Lower Triassic, S-Germany

Christina Schmidt, Benjamin Busch & Christoph Hilgers*

Abstract: The lateral heterogeneity of reservoir rocks is important to assess storage potential and permeability. This case study focusses on a Lower Triassic (upper Olenekian) outcrop of fluvial sandstones of the Plattensandstein Member (Röt Formation) near Röttbach in the southern part of the Germanic Basin, southern Germany. The Buntsandstein Group is considered a suitable reservoir for thermal storage or exploration in southern Germany. In the Röttbach Quarry, the >10 m thick lithic arkoses are exposed over 35 m laterally in three adjacent walls and consist of two units separated by an erosive surface. They are covered by several metres of the Lower Röt Claystone Member. Using sedimentological log ging, spectral gamma ray , porosity and permeability measurements as well as petrographic analyses calculating compac tion parameters, lateral reservoir quality differences are studied.

Sedimentary structures in the multi storey channels suggest a point bar deposit. The migration direction of the channels correlates with deteriorating reservoir quality. This reduction in porosity and permeability correlates with an increased detri tal mica and authigenic illite content, the occurrence of rip up clasts and a lateral increase of gamma ray signatures by 19 API (avg. 5.0 vol% K, 2.7 ppm U, 11.9 ppm Th). The occurrence of larger amounts of mica and clay minerals is linked to decreasing flow velocities throughout the evolution of a meandering system. They enhance compaction and reduce avail able intergranular pore space.

Permeability laterally deteriorates by up to three orders of magnitude (48 to 0.02 mD, avg. 9 mD) while measured po rosities show minor variability (11 to 19 %, avg. 16 %). The deterioration of reservoir quality is related to compactional (COPL 11 to 28 %, avg. 18 %) and cementational porosity loss (CEPL 13 to 29 %, avg. 22 %) and is mainly controlled by detrital mica and authigenic illite.

Kurzfassung: Laterale Heterogenitäten in Reservoirgesteinen sind von Bedeutung bei der Einschätzung von Speicherkapa zitäten und Permeabilitäten. Diese Fallstudie beschäftigt sich mit einem untertriassischen (Oberes Olenekium) Aufschluss fluviatiler Sandsteine der Plattensandstein Subformation (Röt Formation) nahe Röttbach im südlichen Germanischen Be cken, Unterfranken. Die Buntsandstein Gruppe gilt als geeignetes Reservoir für die Wärmespeicherung oder Exploration in Deutschland. Im Steinbruch Röttbach sind die >10 m mächtigen lithischen Arkosen lateral in drei aufeinanderfolgenden Wänden über 35 m aufgeschlossen und bilden zwei durch eine erosive Fläche getrennte Einheiten. Sie werden überlagert von mehreren Metern der Unteren Röttonstein Subformation. Laterale Unterschiede in der Reservoirqualität werden anhand sedimentologischer Logs, Messungen spektraler Gammastrahlung, Porositäts und Permeabilitätsmessungen sowie petro graphischer Analysen einschließlich der darauf basierenden Berechnung von Kompaktionsparametern untersucht.

Sedimenttexturen in den mehrstöckigen Flussrinnen deuten auf eine Gleithangablagerung hin. Die Migrationsrichtung der Rinne korreliert mit abnehmender Reservoirqualität. Diese Abnahme der Porosität und Permeabilität korreliert mit zu nehmenden detritischen Glimmer und authigenen Illitgehalten, dem Auftreten von Tongeröllen und einer lateralen Zunah me der natürlichen Gammastrahlung um 19 API (Ø 5,0 Vol. % K, 2,7 ppm U, 11,9 ppm Th). Das Auftreten größerer Mengen Glimmer und Tonminerale wird durch abnehmende Fließgeschwindigkeiten während der Evolution des mäandrierenden Systems erklärt. Sie verstärken den Prozess der Kompaktion und reduzieren den verfügbaren intergranularen Porenraum.

Die Permeabilität verringert sich lateral um drei Größenordnungen (48 bis 0,02 mD, Ø 9 mD) während gemessene Po rositäten eine geringe Variabilität zeigen (11 bis 19 %, Ø 16 %). Die Abnahme der Reservoirqualität ist gebunden an Poro sitätsverluste durch Kompaktion (COPL 11 bis 28 %, Ø 18 %) und durch Zementation (CEPL 13 bis 29 %, Ø 22 %) und wird hauptsächlich von detritischen Glimmern und authigenem Illit kontrolliert.

Keywords: Triassic red beds, Plattensandstein Member, lateral reservoir quality variation, porosity, permeability, Lower Franconia

Schlüsselwörter: Triassische Rotschichten, Plattensandstein Subformation, laterale Variation der Reservoirqualität, Porosi tät, Permeabilität, Unterfranken

*Address of the authors:
Structural Geology and Tectonics, Karlsruhe Institute of Technology, Adenauerring 20a, 76131 Karlsruhe, Germany (christina.schmidt2@kit.edu)

1. Introduction

Reservoir sandstones of fluvial origin exhibit heterogeneities on multiple scales that are difficult to detect when relying solely on vertical profiles or 1D well information (Miall 1977, 1988a; Miall & Turner-Peterson 1989; Taylor & Ritts 2004; Bridge 2006; Pranter et al. 2007). Porosity and permeability and thus reservoir quality can be controlled by e.g. the overall depositional system, moving down in hierarchy to the fluvial style and the sorting, size and composition of individual sand grains (Miall 1988a, 2014; Bridge 2006; Morad et al. 2010). The categories micro-, meso-, macro- and megascopic heterogeneity have been introduced that cover characteristics observed on the grain scale, the lithofacies scale, the scale of the specific architectural element and the scale of the overall stratigraphy, respectively (Tyler & Finley 1991; Miall 1996). Often core or well data cannot provide the information necessary to identify architectural elements from lithofacies types represented in the sample material or image logs. Additionally, they lack information on lateral changes making it difficult to predict rock properties away from the core sample or well (Miall 1977, 1988a; Miall & Turner-Peterson 1989; Becker et al. 2017). Outcrop analog studies offer a means to assess reservoir quality with respect to micro- up to macro-, sometimes even megascopic heterogeneity displayed in 2D or 3D along outcrop walls utilizing thin sections, plug samples and macroscopic observations (Miall 1988a; Wachutka & Aigner 2001; Bridge 2006; Pranter et al. 2007; Trendell et al. 2012; Becker et al. 2017).

Heterogeneity of bedsets may include the detrital composition, authigenic alteration, sedimentary structure, or texture (Pranter et al. 2007; Trendell et al. 2012). Volumes of quartz cement often correlate negatively with grain coating coverages on detrital grains (Heald & Larese 1974). The extent of grain coating coverage at grain contacts was also recently related to the degree of chemical compaction (Monsees et al. 2020). Compaction is facilitated by both mechanical (grain rearrangement and deformation) and chemical compaction (pressure dissolution of e.g. quartz grains, Bjørkum et al. 1993; Walderhaug 1996). A higher amount of ductile clasts among the detrital framework grains (e.g. micas or shale rock fragments) enhances mechanical compaction. Ductile clasts may form a pseudomatrix as they undergo strong deformation during compaction(Geyer 2005; Bertier et al. 2008; Molenaar et al. 2015; Henares et al. 2016a; Becker et al. 2017; Busch et al. 2019). In diagenetic systems with early cementation, mineral growth of authigenic phases such as feldspar and carbonate may stabilize the grain framework against mechanical compaction during subsidence, and may further enhance reservoir quality when dissolved at depth (Scherer 1987; Canham et al. 1996; Walderhaug 1996, 2000; Paxton et al. 2002; Lü et al. 2015; Henares et al. 2016b; Line et al. 2018). The distribution of detrital clay and mica minerals in the mineral framework causes a reduction of reservoir quality for similar rock types affected by the same subsidence history (Gaupp et al. 1993; Walderhaug 2000; Lander et al. 2008; Morad et al. 2010; Fischer et al. 2012; Busch et al. 2017, 2020). During chemical compaction, mineral dissolution and precipitation impacted by increased contents of mica and clay minerals significantly change the pore volume and its connectivity (Lundegard 1992; Bjørkum et al. 1993; Gaupp et al. 1993; Paxton et al. 2002; Morad et al. 2010; Beyer et al. 2014; Bjørlykke 2014; Monsees et al. 2020). Authigenic phases such as feldspar-, carbonate- or quartz cements that reduce pore space mostly deteriorate reservoir quality. Authigenic clay minerals like kaolinite or illite reduce permeability and porosity during early and burial diagenesis (Bjørkum et al. 1993; Gaupp et al. 1993; Walderhaug 1996, 2000; Lander & Walderhaug 1999; Morad et al. 2010; Taylor et al. 2010; Bjørlykke 2014).

Petrophysical properties may vary in fluvial deposits by several orders of magnitude. Doyle & Sweet (1995) measured porosities of 5.4 % to 30.4 % and permeability ranges over six orders of magnitude within a 15 m × 35 m outcrop representing stacked meander channels. They proposed the lithofacies type as reservoir quality-controlling factor. For example, main vertical permeability-reducing baffles present as mud clast lags at the channel base and mud drapes on lateral accretion surfaces (Doyle & Sweet 1995). Permeability variations over three orders of magnitude were also recognized on a scale of <3 m for braided channel sandstone beds (McKinley et al. 2011), linked to the type of underlying erosional bounding surface and the successive deposition. Depositional parameters (grain size, sorting) controlled petrophysical properties above scour troughs, whereas in continuous channel fill deposits diagenetic cements reduce reservoir quality (McKinley et al. 2011). Equal variability has been observed in composite point bar deposits. Here, permeability reduction was linked to a cemented mud horizon connected to the floodplain generated during channel abandonment (Hartkamp-Bakker & Donselaar 2009). Differences between fore- and bottomsets have been determined with bottomsets of lower permeabilities due to smaller grain size and poorer sorting (Hartkamp-Bakker & Donselaar 2009). Becker et al. (2017) showed permeability changes from 0.001 to 0.1 mD on a larger scale over a horizontal profile of 150 m in a single fluvial sandstone coset related to cm-scale fining-upwards grading and internal erosion surfaces.

In this study, lateral variations in sandstone composition, porosity and permeability of a macroscopically homogenous fluvial Lower Triassic Buntsandstein deposit on the outcrop scale are studied. Petrophysical heterogeneities of the fluvial sandstones evolving with progressive lateral accretion at a point bar in a meandering river system are presented. The effect of meander evolution influencing the detrital and authigenic mineral contents is discussed. The main reservoir quality controls due to detrital and authigenic compositions and their effect on compaction are presented.
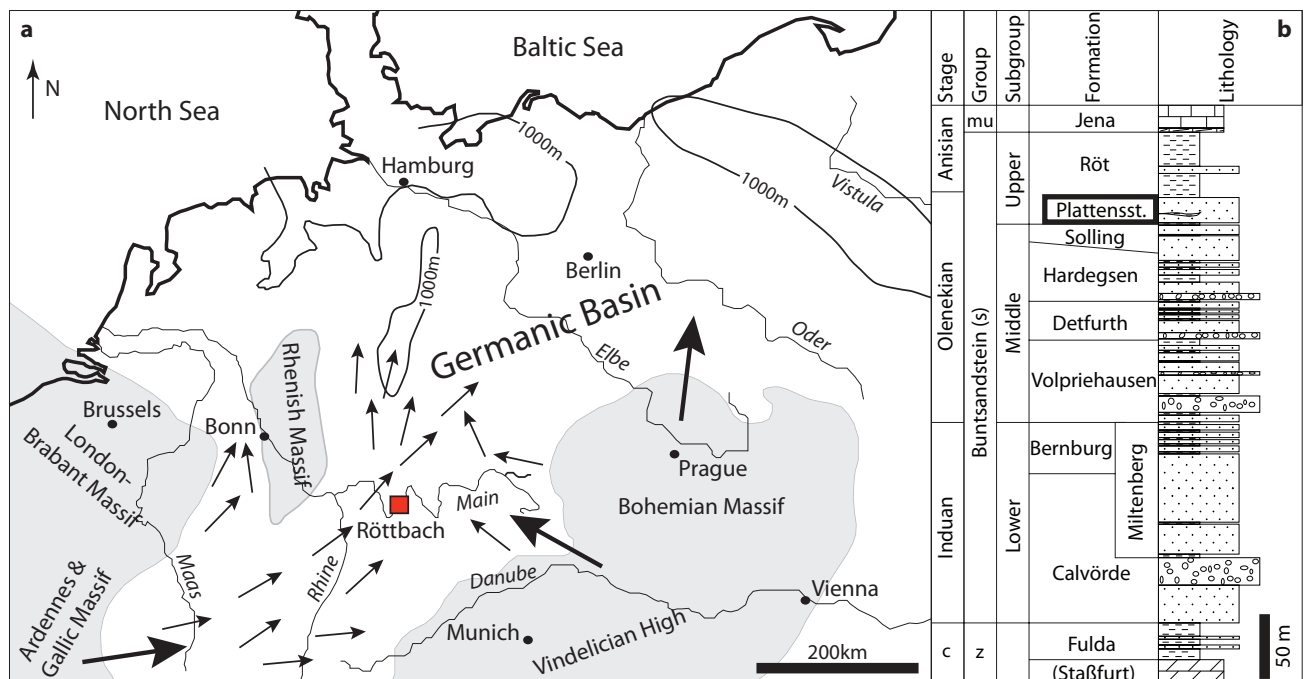
2. Geological setting

The outcrop in Röttbach, 5 km north of Wertheim, Lower Franconia, southern Germany, features red fluvial sandstones of the Lower Triassic (late Olenekian) Platten-

sandstein (Röt Formation, Upper Buntsandstein) (Deutsche Stratigraphische Kommission 2016; Menning 2018; Röhling et al. 2018; Fig. 1). Those deposits are part of the southwestern marginal facies of the southern extension of the Germanic Basin, where the Buntsandstein extends over approximately 600 km from the Burgundy Basin to the Centre of the Germanic Basin (Backhaus 1974; Ziegler 1990; Hagdorn et al. 2009; Okrusch et al. 2011; Freudenberger et al. 2013; Fig. 1a). Of the 530 m thick Buntsandstein succession in Lower Franconia, 25 to 35 m are Plattensandstein in the study area (Freudenberger 1990; Geyer 2002; Bock et al. 2005). The Plattensandstein contains intercalations of claystone, which account for approximately 10 to 20 % of the overall rock unit in the region (Freudenberger 1990). The epicontinental basin formed by minor thermal subsidence rates and ongoing sedimentation during the Triassic (Röhling & Lepper 2013; Meschede & Warr 2019). Sedimentation was mainly controlled by local palaeotopography (Schröder 1982; Hagdorn et al. 2009; Röhling & Lepper 2013; Röhling et al. 2018). The detritus was shed from the Vindelician High from the southeast and the Ardennes and Gallic Massif in the west, while the overall transport took place to the northeast (Backhaus 1974; Ziegler 1982; Schultz-Krutisch & Heller 1985; Geyer 2002; Bock et al. 2005; Hagdorn et al. 2009; Freudenberger et al. 2013; Röhling & Lepper 2013; Röhling et al. 2018; Meschede & Warr 2019; Fig.1a).

The marginal facies developed from braided rivers in the Early and Middle Buntsandstein (Induan to early Olenekian) to meanders in the Upper Buntsandstein (late Olenekian; Geyer 2002; Bock et al. 2005; Okrusch et al. 2011; Freudenberger et al. 2013), the latter being exposed in the quarry. Corresponding channels of the Upper Buntsandstein form shallow incisions of up to a few metres in depth and meander laterally over a substantial width but at a relatively constant position (Geyer 2002; Bock et al. 2005; Okrusch et al. 2011; Freudenberger et al. 2013). The Plattensandstein itself represents meandering river systems shedding sediment in a low-relief area with occasional flooding events (Geyer 2002; Bock et al. 2005). Plant and trace fossils document a mainly terrestrial setting (Kirchner 1927; Trusheim 1937; Geyer 2002) but horizons of marine bivalves reaching into the Odenwald area imply a marine influence already in the Plat-

Fig. 1: (a) Location of the study area (red square) in the Germanic Basin during the Lower Triassic. Sediment transport (indicated by arrows) from the Vindelician , Gallic and Ardennes highs (after Geyer et al. 2011; Ziegler 1990). Isopachs display the maximum sediment thicknesses for the Buntsandstein, Lower Triassic, in the wider region. (b) Local stratigraphy: The Plattensandstein Member (black square) is present in the footwall of the Lower Röt Claystone Member, Röt Formation (Upper Buntsandstein Subgroup, upper Olenekian); after Okrusch et al. (2011) modified from Geyer (2002).

tensandstein and in the subsequent Röt Claystones (Frank 1937; Martini 1992; Geyer 2002).

The upper stratigraphic succession exposed in the quarry consists of Lower to Middle Triassic (late Olenekian to Anisian) Lower Röt Claystones (Upper Buntsandstein), which were deposited in a sabkha or playa environment (Aigner & Bachmann 1992; Okrusch et al. 2011). Prevailing lithologies are silt- and claystones, which may feature salt or sulphate nodules (Okrusch et al. 2011; Meschede & Warr 2019). This reflects the intermittent ingression of the Tethys Ocean from the south in the Upper Buntsandstein, at the transition from the Lower to Middle Triassic (Backhaus 1981; Schröder 1982; Ziegler 1982; Aigner & Bachmann 1992; Okrusch et al. 2011; Freudenberger et al. 2013). Warm, humid climates during the Tertiary could have led to intense weathering and pedogenesis in preceding formations (Böse et al. 2018).

3. Materials and methods

Along three profiles of vertically stacked sandstone beds extending along 35 m, 1-inch-diameter plugs were drilled parallel to bedding (N = 36; Fig. 2a). The three sampled profiles originated from two beds separated by a subhorizontal erosional surface. Generally, the bedding was poorly visible in the active quarry due to the extraction method combining a rope-saw system with vertical drill holes. Profile 1 was the basal profile with distances between 1.60 m and 2.50 m from the top contact to the overlying claystone, situated at a central position in the basal unit (N = 14; Fig. 2a). Profile 2 was sampled 0.30–0.45 m above profile 1 and within the same unit (N = 14). In its hanging wall profile 3 was located in the subsequent bed, 0.75–1.20 m above profile 1 (N = 8). In each profile two samples originated from the SE-wall (orientation: 320/90°) and two from the NW-wall (orientation: 126/82°), all others were extracted from the SW-quarry wall. The 24 samples from the SW-wall were plugs of one horizontal direction, whereas the remaining 12 samples from the SE- and NW-wall represented a second, subperpendicular horizontal direction. The produced one-inch plugs were sawed to lengths between 2.5 to 4.0 cm. Trim ends were used for thin section preparation.

Bounding surfaces of fluvial origin were classified according to Miall (1988a, 1988b). Six orders were subdivided based on concordance of set bedding contacts, changes in direction of deposition, erosion, facies assemblages and architectural elements (Miall 1985), concordant sand sheet contacts, and contacts between stratigraphic units.

Porosity and permeability were measured on 1-inch plugs, which were oven dried at 40 °C for one week. The semi-automated micromeritics Accupyc II 1340 helium pycnometer was used for porosity measurements. Horizontal permeabilities were determined in a semi-automated isostatic flow cell of the Fancher type (model Rieckmann) using single-phase gas flow. Compressed air (measured viscosity η = 1.82 × 10⁻⁵ – 1.84 × 10⁻⁵ Pa · s) was used as the permeant while a confining pressure of 1.2 MPa was applied. Permeabilities were calculated from the flow rates according to

Darcy's law and were Klinkenberg-corrected for slip flow (Klinkenberg 1941; Rieckmann 1970).

Trim ends were oven dried at 40 °C for a week and embedded in a blue-dyed epoxy and prepared to a thickness of 30 μm. A combined staining of Alizarin Red S and potassium ferricyanide in HCl was applied to aid in the identification of carbonate minerals. Iron-free dolomite shows no stain from the treatment with this solution (Dickson 1966).

For grain size analyses the long axes of 100 detrital grains were measured for each thin section on a grid adjusted to the largest grain size (Busch et al. 2018). Grain size classes were assigned according to the Udden-Wentworth scale (Udden 1914; Wentworth 1922), sorting was classified after Folk & Ward (1957). Grain roundness was classified using comparative images after Füchtbauer (1988).

Point counting was performed with 300 steps per sample on a grid adjusted to the maximum grain size using a semi-automated Pelcon point counter mounted on a Leitz Aristomet microscope. Results were plotted after Folk (1980). Errors on point counted mineral phases were determined via the half-width of the lower and upper 95 %-confidence bounds as proposed by Howarth (1998). Point count values were rounded to derive a lower and upper bound for each sample. Samples RB-17 and RB-19 contained rip-up clasts with sizes of several mm, which would have skewed the overall area-weighted results during point counting and were not considered for grain size assessments and point counting. All observed types of iron oxide (pore-lining and filling, grains, iron-rich pseudomatrix) were combined in a single class for point counting. As ductile deformation during compaction prohibited any clear distinction between authigenic and detrital iron oxide phases, the point counted class was assigned to the detrital components.
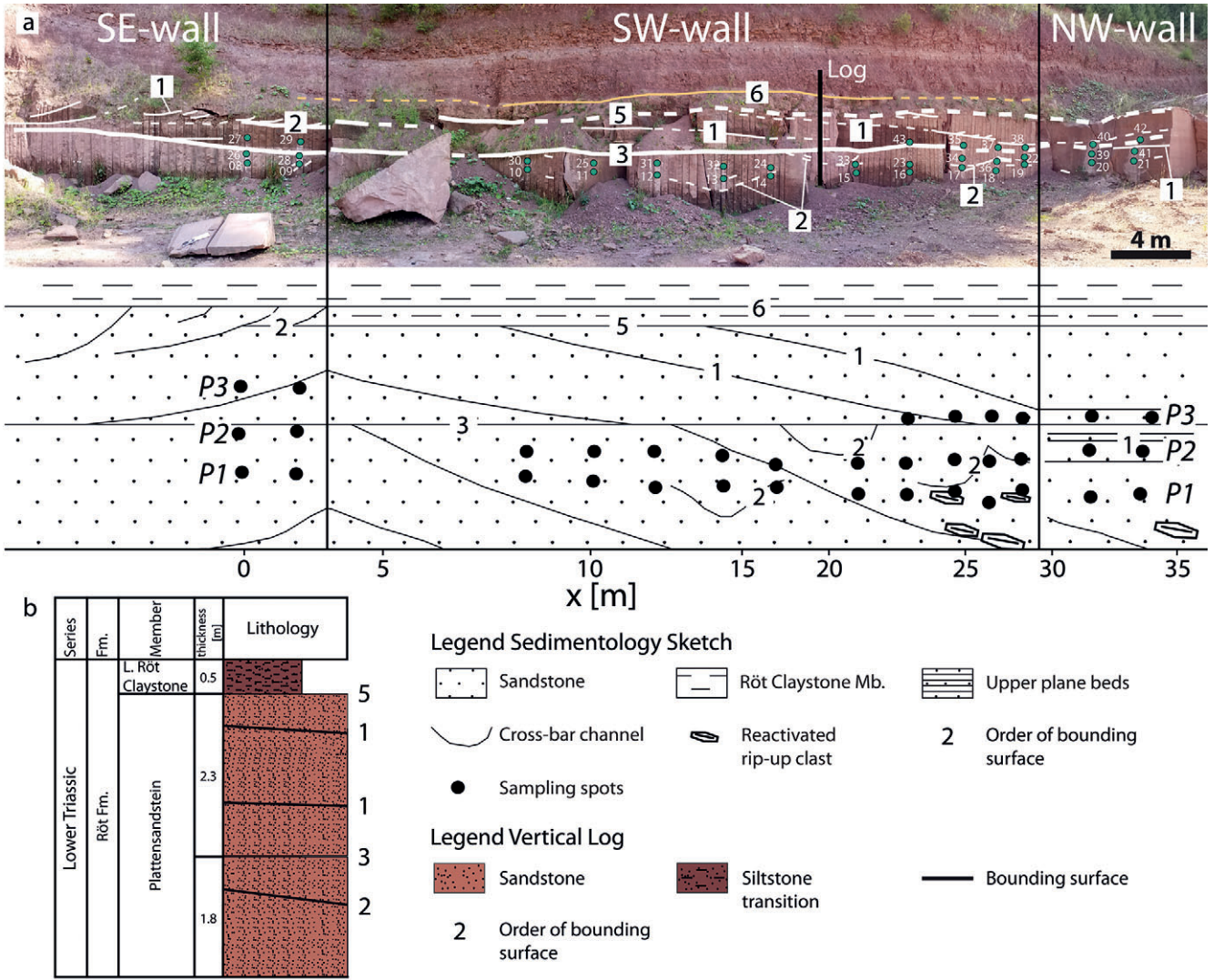
Optical porosity was generally lower than measured porosity since microporosity in clays could not be sufficiently detected in petrographic analyses. To account for microporosity, point counts for kaolinite, chlorite and illite were multiplied with mean fractions of microporosities in those mineral phases after Hurst & Nadeau (1995) and the average of those values was adopted for undifferentiated clay minerals. The calculated microporosity and the point counted inter- and intragranular pore space were combined in the category "point counted porosity".

The intergranular volume (IGV) was calculated according to Paxton et al. (2002) to assess compaction based on point counting results. It comprises the intergranular pore space, intergranular cement volumes and the depositional matrix (Eq. 1). By calculating the minus-cement porosity after Lundegard (1992), adding up optical porosity and intergranular cement volume, the amount of porosity loss due to compaction (COPL) or cementation (CEPL) could be determined following equations 2 and 3.

$$IGV = \phi_{intergr.} + V_{cement} + V_{matrix} \qquad \text{Eq. 1}$$

$$COPL = \phi_{initial} - \frac{(100 - \phi_{initial}) \times IGV}{100 - IGV} \qquad \text{Eq. 2}$$

Fig. 2: (**a**) Panorama photo of the studied quarry and the corresponding, vertically exaggerated sedimentological sketch (orientation changes are indicated by the vertical black lines; dashed and solid white lines indicate interpreted structures). Three profiles (P1 to P3) were sampled along the SE , SW and NW wall of the active quarry (black dots). The Spectral gamma ray (SGR) profile was measured along P1. The orange line, 6, highlights the border between the Plattensandstein and the Lower Röt Claystone Member (both Röt Formation) in the hanging wall (s. Fig. 1b). Numbers indicate the order of the observed bounding surface after Miall (1988a). White lines follow sedimentary structures as coset boundaries, tangential cross bed sets and minor channels etc. and are drawn as dashed lines where poorly visible. (**b**) Vertical log (location in [a]) showing the stratigraphy, lithology and visible sedimentary structures.

$$CEPL = (\phi_{initial} - COPL) \times \frac{V_{cement}}{IGV} \qquad \text{Eq. 3}$$

Variables are the initial porosity $\phi_{initial}$, the present-day point counted values for the intergranular porosity $\phi_{intergr.}$, the cement volume V_{cement} as well as the matrix volume V_{matrix} for each sample. The initial porosity in a fluvial system was assumed to be 45 % after Wilson & McBride (1988).

Spectral gamma ray (SGR) was measured at 14 spots along profile 1 using the hand-held, auto-stabilizing spectrometer RS-230 BGO Super-SPEC. The device detects potassium, uranium and thorium decays over a time span of three minutes and calculates element contents. Results are

given in API units, calculated after Rider & Kennedy (2011; Eq. 4).

$$SGR\ (API) = 16.32\ API \times K(\%) + 8.09\ API \times \\ U\ (ppm) + 3.93\ API \times Th\ (ppm) \qquad \text{Eq. 4}$$

The error of 3.4 % on the API value was determined as the standard deviation of 10 measurements of the same sandstone sample.

4. Results

Sedimentological logging

The up to 10 m high outcrop is composed of two subhorizontal red sandstone beds with decimetre to two metre thick cosets (Fig. 2a). Macroscopically, only few sedimentary structures are recognizable in the outcrop and included in the sedimentological sketch and log (Fig. 2). Coset boundaries in the study area coincide with third-order bounding surfaces after Miall (1988a). Third order surfaces erode underlying strata at a low angle and exhibit similar facies assemblages underneath and on top of the surface (Fig. 2: no. 3). Some sets within the cosets are pinching out to the NW and their outlines correspond to first-order bounding surfaces of equivalent bedforms (Fig. 2: no. 1). Tangential foresets of the SE-wall may reach angles of 20° (Fig. 2a: no. 1), whereas the base and top boundaries bracketing single cosets mainly exhibit a shallow or subhorizontal dip (Fig. 2: no. 3).

The basal, up to 1.8 m thick bed consisting of fine-grained sandstone (profiles 1 and 2) shows two channel-like concave-up surfaces in the SW-quarry wall of 2 and 4 m width (Fig. 2: no. 2). They are classified as second-order surfaces because of an apparent change in flow direction. The same basal bed exposes more strongly inclined (up to 20°) foresets in the SE-wall. It is overlain by an up to 1.2 m thick bed, which consists of similar fine-grained sandstone. Both units are separated by an erosive surface (Fig. 2: no. 3). This third-order surface marks the upper limit of the basal coset with the overlying one exhibiting the same apparent dip direction. The upper bed displays few shallowly (<10°) dipping surfaces on the NW-wall and some strongly inclined, tangential surfaces on the SE-wall (concave-up white lines; Fig. 2a: no. 1)). The SW-wall exposes two surfaces of very shallow apparent dip to the NW, that behave asymptotic towards the base of the bed, continuing each for >10 m (Fig. 2: no. 1). Those recurring first-order surfaces mirror the shallowly NW-dipping surfaces present in the basal coset. All of those surfaces outline sigmoidal sandstone units. The transition to the Röt Claystone Member in the hanging wall is constituted by a 0.5 m thick, weathered unit of silt- to sandstone at the SW-wall, which is separated from the underlying sandstone unit by a discrete horizontal erosive surface truncating sedimentary structures of the footwall (Fig. 2: no. 5). The bounding surface was classified as fifth-order because it limits a major sand sheet deposit in its footwall (Fig. 2: no. 5). At the SE-wall another 0.4 m thick sandstone coset is present, separated from the underlying sandstone by another second-order bounding surface between the two cosets (Fig. 2a: no. 2). The overall silty to sandy lithology is then overlain by the claystones of the Röt Claystone Member separated by a sixth-order bounding surface tracing mappable stratigraphic units (Fig. 2a: no. 6).

Irregular, reddish-brown, elongated, angular rip-up clasts of up to 7.5 cm are observed in mined blocks and the exposed basal sandstone coset and appear predominantly in the NW-part (sketch, Fig. 2a). They consist of clayey to silty material and exceed the thin section-scale in length in two samples (RB-17, RB-19). Millimetre-scale mica flakes are ubiquitous on all bedding planes. No tropical weathering or other types of palaeosol can be identified in the outcrop.

Petrography
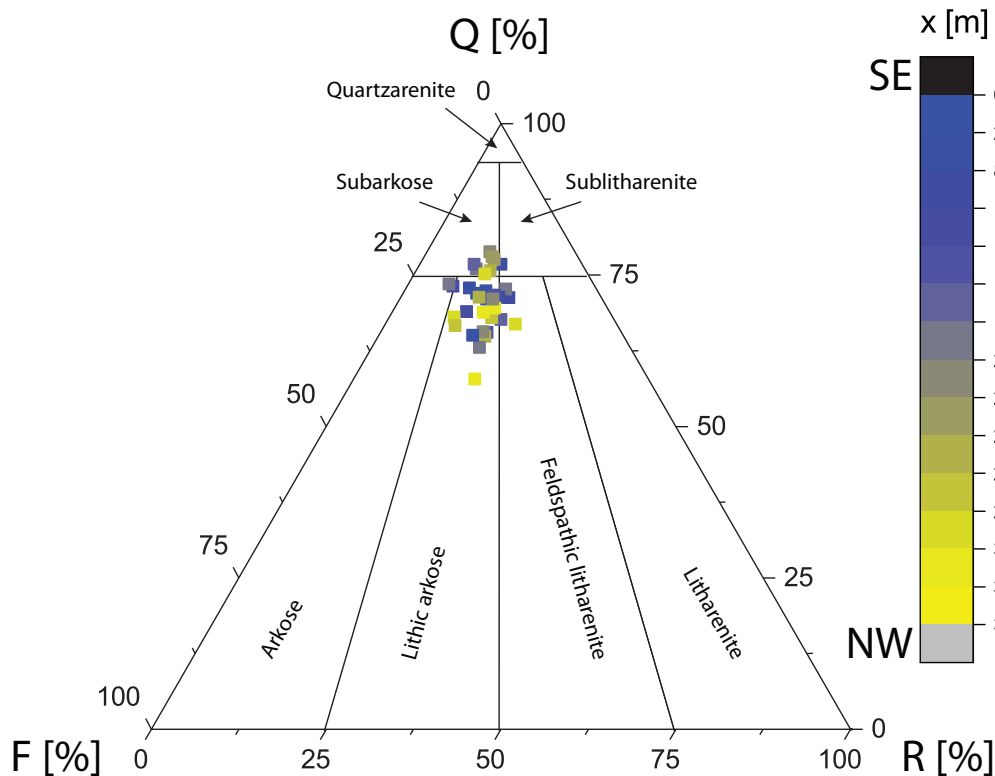### Detrital composition

The samples are classified as lithic arkoses (N = 21), sub-arkoses (N = 8), feldspathic litharenites (N = 3) and arkoses (N = 2) (Fig. 3). The average quartz grain content is 35 vol% (max. 41 vol%, min. 23 vol%) (Supplementary Table). The average feldspar grain content is 8 vol% (max. 12 vol%, min. 6 vol%), while rock fragments amount to 6 vol% (max. 9 vol%, min. 3 vol%) (Supplementary Table). The observed lithology consists of very fine- (N = 8) to fine-grained (N = 26) sandstone with average grain sizes of 110 to 170 μm (avg. 150 μm). The sand grains are subangular to sub-rounded and moderately (N = 33) to well sorted (N = 1) (Supplementary Table). Grains are sometimes aligned while micas always adjust their long axes parallel to bedding planes. From qualitative assessment, grain contacts are primarily concavo-convex contacts with only few sutured and point contacts indicating well compacted sandstone.

The major detrital component quartz is present as mono- and polycrystalline grains frequently displaying undulose extinction. Feldspars are mostly K-feldspars, plagioclases are rarely preserved and not encountered during point counting. K-feldspars are often partially dissolved. Rock fragments include sandstone, plutonic and metamorphic rock fragments, phyllite, chert, ductile siltstone, claystone and shale fragments (Fig. 4a) and may show partial dissolution. The intragranular pore space in feldspars and rock fragments only contributes up to 3.3 vol% (avg. <1 vol%) and does not significantly increase the overall point counted porosity (avg. 13 vol%, max. 17 vol%, min. 9 vol%) (Supplementary Table).

Mineral grains include mica, primarily muscovite and some biotite adding up to on average 2.1 vol% (max. 8.7 vol%, min. 0.3 vol%; Fig. 4b) and accessory minerals as zircon, tourmaline and opaque and heavy mineral grains combine to a maximum of 1 vol% in each sample. Iron oxides are present in all samples and occur as pore-lining and filling phases, grains, and iron-rich pseudomatrix with on average 14 vol% (max. 21 vol%, min. 6 vol%; Fig. 4e). Some of the red sandstone samples contain greyish white bleached zones as speckles or bleached laminae.

Reddish-brown rip-up clasts occur as highly deformed hematite-rich shaly siltstone fragments in two thin sections in the NW of the outcrop (RB-17, RB-19; Fig. 4c). Detrital matrix was not encountered during point counting.

The iron oxide contents in the SE-part are below the mean, while higher contents are present in the NW-part (Fig. 5a). The contents of detrital mica increase towards the NW-part (Fig. 5b). The grain sizes show an insignificant deviation from the average grain size of 150 μm along the profiles (Fig. 5c). Similarly, correlations are poor for vertical variations in grain size, iron oxide- and mica contents. The few recognizable sedimentary structures do not appear to correlate with e.g. mica contents (Fig. 2a). An above-average mica content in a sample originating from the small channel

Fig. 3: QFR plot of the sandstone samples (N   34) from the three profiles in the studied Plattensandstein outcrop, Röt Formation (blue   SE part of the outcrop, yellow   NW part of the outcrop).

in the basal coset (red, RB-13) is opposed by a below-average value for the overlying sample within the same channel structure (orange, RB-32, Fig. 2a, 5b at x = 14.7 m).
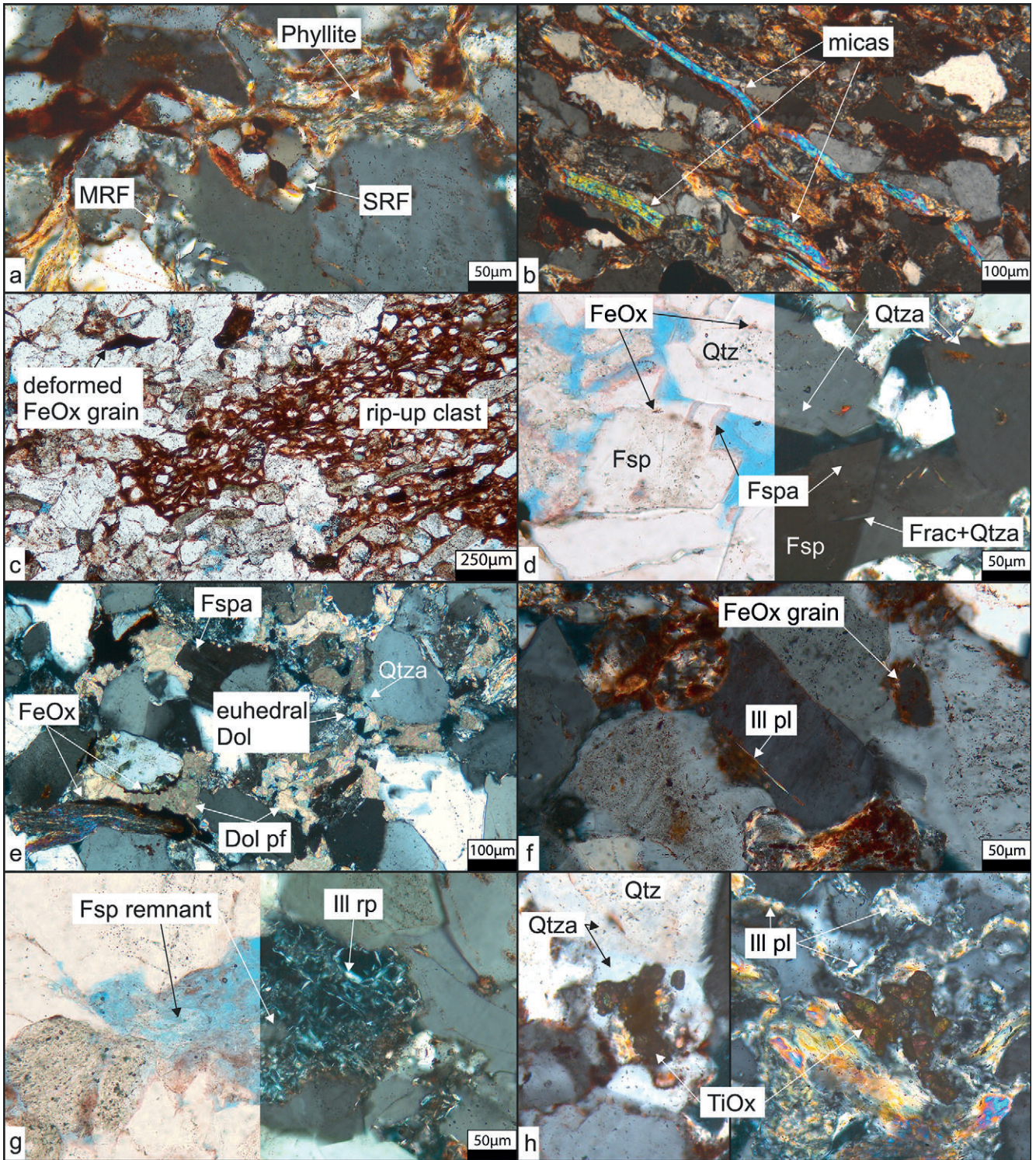
Authigenic phases
The most common authigenic mineral in the study area is quartz with on average 15 vol% (max. 20 vol%, min. 7 vol%; Figs. 4d, e). Other blocky, pore-filling cements are feldspar with on average 5 vol% (max. 8 vol%, min. 2 vol%; Figs. 4d, e) and occasionally dolomite (avg. 0.2 vol%, max. 1.3 vol%, min. 0 vol%; Fig. 4e). Feldspars often formed euhedral cements, which occasionally stop neighbouring quartz cements and prevent their development into a euhedral overgrowth (Fig. 4d). A fracture in a euhedral feldspar overgrowth is filled by quartz cement from a neighbouring detrital grain (Fig. 4d). Dolomite cements often appear with a pitted crystal outline or are partially dissolved. They form localized pore-filling patches with a diameter of up to several hundreds of μm (Fig. 4e). Those completely pore-filling dolomite textures enclose detrital grains without any overgrowth cements and appear to prevent the formation of long grain contacts during compaction (Fig. 4e, left). Furthermore, some dolomites show euhedral rhombs, which fill pores and also replace feldspar cements (Fig. 4e, top). The dolomite rhombs may occur on euhedral feldspar and quartz cements (Fig. 4e, top).

Illite is present both as a pore-lining and a pore-filling phase with on average 7 vol% (max. 16 vol%, min. 2 vol%;

Figs. 4f, h). The pore-lining phase is present as a grain coating. Minor amounts of kaolinite (avg. 0.03 vol%) occur as pore-filling booklets in some samples filling intergranular pores, sometimes together with illite fibres. Authigenic titanium oxides (TiOx) are present as clusters of small anhedral aggregates in the pore space (avg. 0.1 vol%; Fig. 4h). Some authigenic minerals also replace existing grains, such as illite replacing feldspars (avg. 1 vol%, max. 3 vol%, min. 0 vol%; Fig. 4g) and subordinately kaolinite as well as chlorite replacing micas and rock fragments (avg. 0.2 vol%, max. 1.0 vol%, min. 0 vol%). Kaolinite has been rarely encountered as a replacive phase throughout petrographic analyses but was not registered during point counting.

Lateral variation of quartz cement contents (avg. 15 vol%, max. 20 vol%, min. 7 vol%) along the profiles is small with lower mean values for the three samples in the NW-part (11 to 15 vol%; Fig. 6a, black dots). Illite volumes scatter around the average value of 7 vol% (max. 16 vol%, min. 2 vol%; Fig. 6b). The mean values for five sample locations in the SE mostly plot below average (4 to 7 vol%). Comparably high values for five samples of the NW-part are encountered (8 to 10 vol%) with one exception of 6 vol% mean illite content at 31.7 m. Furthermore, the amount of illite volumes exhibits a broader spread in the NW than in the SE along the profile (Fig. 6b). This is similar to observations in the cross-plot of mica contents (Fig. 5b). The scatter plot displaying feldspar cement contents along the profiles shows no deviation of data from the average (Fig. 6c). The indicated correlation between

sample position and illite content cannot be linked to sedimentary structures. Four samples from the NW of the outcrop (RB-35, -37, -38, -43), all originating from the same coset with shallowly NW-dipping sets in the topmost profile (blue; Fig. 6), plot above and below the average value.

Spectral gamma ray

Calculated API values along profile 1 range from 135.8 to 169.2 API (Fig. 7). Data generally increase from the SE to the NW. With two exceptions of roughly average gamma ray values (RB-01 at 0 m and RB-05 at 12 m) all samples located between 0 m and 22.7 m lie below the average gamma ray value of 150.1 API whereas all following samples from 24.7 m with one exception (RB-18 at 26 m) are characterized by above-average values. The first high spectral gamma ray reading coincides with the plug sample containing rip-up clasts (RB-17, x = 24.7 m). Further towards the NW SGR-values decrease (x = 26.7 m) before attaining continuously high values again from sample RB-19 on, which contains a rip-up clast (x = 28.7 m). Sedimentary structures, e.g. the channel structure in the SW-wall (RB-13; Fig. 2a), apparently do not affect the SGR values. None of the extrema of the SGR-plot corresponds to a specific type of sedimentary structure. Absolute values are on average 5.0 vol% K, 2.7 ppm U, 11.9 ppm Th. In the SE, values are at 4.8 vol% K, 2.8 ppm U, 12.6 ppm Th and reach up to 5.1 vol% K, 3.1 ppm U and 15.5 ppm Th in the NW (Supplementary Table).

Fig. 4: (**a**) Overview of rock fragments, e.g. a sandstone rock fragment (SRF), metamorphic rock fragment (MRF) and a deformed phyllite clast (RB 24, xpl). (**b**) Kinked/deformed detrital mica flakes aligned to the bedding (RB 21, xpl). (**c**) Rip up clast from the NW part of the studied outcrop and deformed FeOx grains (RB 19, ppl). (**d**) Syntaxial quartz overgrowths (Qtza) limited in their growth by euhedral feldspar cement (Fspa), each on the respective substrate grain (Qtz, Fsp) partially enclosing reddish brown remnants of a hematite dust rim (FeOx). A fracture in a feldspar grain and overgrowth contains quartz cement from the neighbouring detrital grain (Frac + Qtza, RB 26, ppl   left, xpl   right). (**e**) Dolomite cement (Dol) sometimes occurs pore filling directly around detrital quartz and feldspar grains without syntaxial overgrowths, e.g. to the left of the image (Dol pf). However, in the upper half of the image it encloses authigenic quartz and feldspar cements (Qtza, Fspa) and develops euhedral rhombs. FeOx occurs as pore lining phase on detrital grains (RB 28, xpl). (**f**) Pore lining illite (Ill pl) on a detrital grain and underneath authigenic cement as well as reddish hematite pigments and iron oxide grains (RB 13, xpl). (**g**) Illite replacing a former feldspar grain with only grain remnants and hematite pigments visible (Ill rp, RB 26, ppl   left, xpl   right). (**h**) Two examples of authigenic titanium oxide (TiOx) forming subhedral crystal aggregates in the intergranular volume. On the left TiOx is encased in quartz cement (RB 25, xpl). On the right the aggregates fill the intergranular volume, which also features abundant pore lining illite fibres (RB 06, xpl).

Porosity and Permeability

Porosities (Φ) of 36 plugs range from 10.5 to 18.8 % (avg. 15.5 %; Supplementary Table). Permeabilities (k) range from 0.02 to 48.43 mD (avg. 9.19 mD; Supplementary Table). The porosity-permeability scatter plot (Fig. 8) exhibits a good correlation between porosity and permeability. Overall, both porosity and permeability become smaller and reach 10.5 % and 0.02 mD, respectively, to the NW (Fig. 8).

In profiles 2 and 3 porosities are close to the average value of 15.5 % (Figs. 9a, b). The largest decrease by more than 5 % is shown in the NW-part of the basal profile 1 (Fig. 9c).

In profiles 1 and 3, permeabilities vary by about one order of magnitude between 0 to 22.7 m (Figs. 10a, c). Starting at 24.7 m permeabilities drop by one order of magnitude with overall k <1 mD between 28.7 m and 33.7 m. Profile 2 exhibits very low permeability at 16.2 m (RB-24, 0.34 mD; Fig. 10b) and a sample at 28.7 m that slightly exceeds 1 mD (RB-22, 1.20 mD) but generally matches a permeability decrease toward the NW.
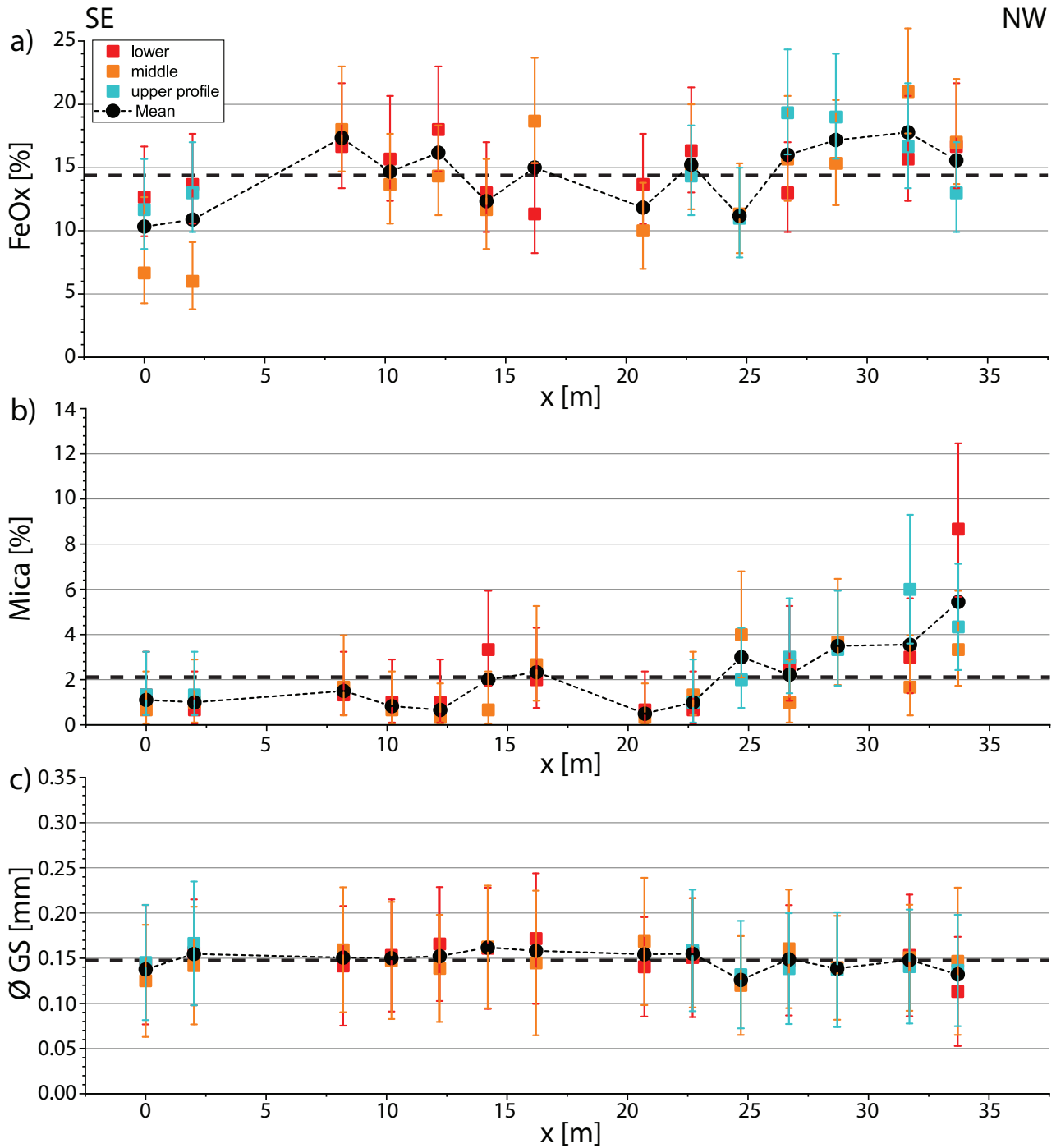
Correlation of reservoir quality controls

To assess the impact of detrital and authigenic constituents on porosity and permeability, scatter plots coded for the content of constituents were created (Fig. 11). An increase in bubble size represents an increase in content. Iron oxides correlate poorly with porosity or permeability (Fig. 11a). However, with increased detrital mica content porosity and permeability are reduced (Fig. 11b). The cross-plot for authigenic quartz indicates higher porosities and permeabilities with slightly increased cement volumes (Fig. 11c). Higher illite contents correlate with lower porosities and permeabilities (Fig. 11d).
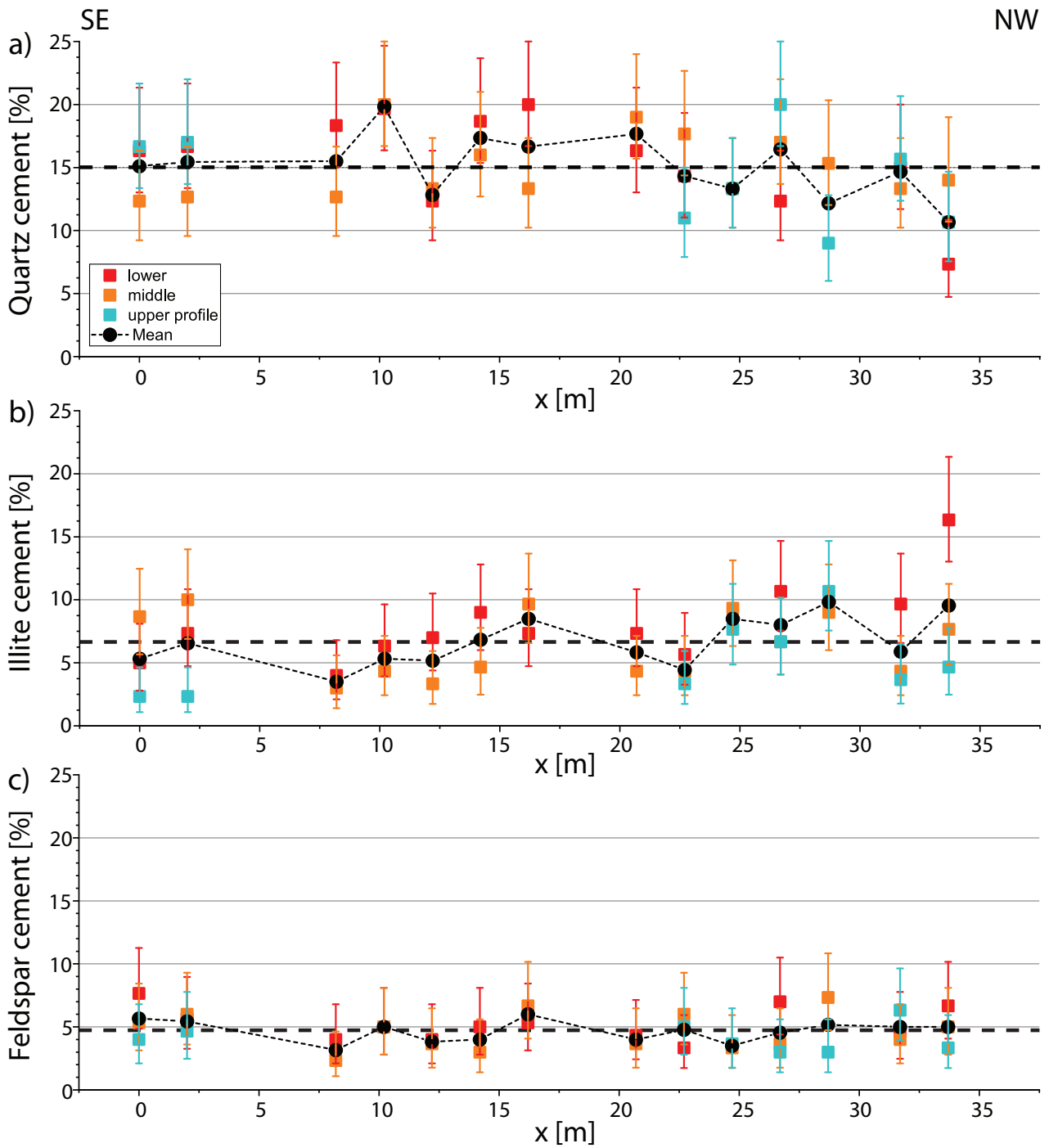
Compaction

The average IGV in the studied samples is 33 % (max. 38 %, min. 24 %). Compactional porosity loss (COPL) is on average at 18 % (max. 28 %, min. 11 %) and cementational porosity loss (CEPL) is at 22 % (max. 29 %, min. 13 %). To assess if there is a general correlation of enhanced compaction or cementation deteriorating reservoir quality along the sampled profiles, COPL is plotted against CEPL after Lundegard (1992; Fig. 12). 25 out of 34 samples lose porosity primarily via cementation (Fig. 12). The plot shows a poor correlation between the position along the profile from NW to SE and COPL or CEPL (Fig. 12).

Laterally, the plots for IGV, compactional and cementational porosity loss do not show a coherent correlation between COPL-/CEPL-values and the position along the profile from SE to NW (Fig. 13). Only the samples from the SE- and NW-sides and their mean for IGV distinctly plot above (+2-3 %, SE) and below average (-3-4 %, NW) (Fig. 13a). Similarly, the COPL-values plot below average in the SE (-3 %) and above average in the NW (+3-4 %; Fig. 13b).
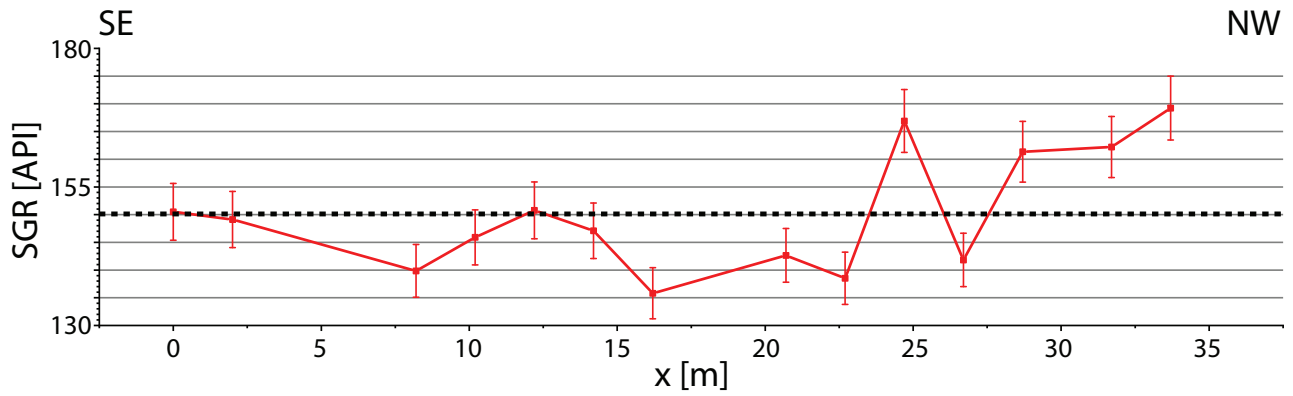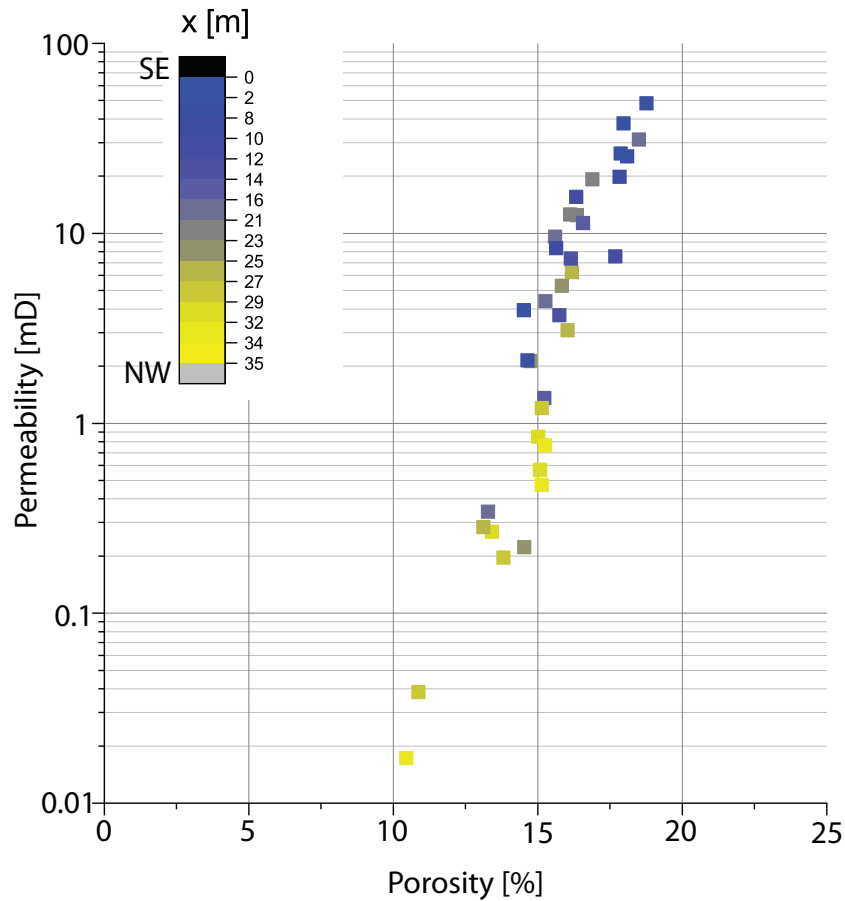
Fig. 5: Scatter plots along the quarry wall from SE to NW for all profiles (dashed line average value; dotted line mean of the three samples at position x). (**a**) Lateral variation of the iron oxide content (FeOx, Ø 14 vol%, max. 21 vol%, min. 6 vol%). (**b**) Lateral variation of the mica content (Ø 2.1, max. 8.7 vol%, min. 0.3 vol%). (**c**) Lateral variation of the average grain size for all samples (GS, Ø 0.150 mm, max. 0.170 mm, min. 0.110 mm).

Fig. 6: Scatter plots along the quarry wall from SE to NW for all profiles (dashed line — average value; dotted line — mean of the three samples at position x). (**a**) Lateral variation of the quartz cement contents (avg. 15 vol%, max. 20 vol%, min. 7 vol%). (**b**) Lateral variation of the illite contents (avg. 7 vol%, max. 16 vol%, min. 2 vol%). (**c**) Lateral variation of the feldspar cement contents (avg. 5 vol%, max. 8 vol%, min. 2 vol%) for all samples.
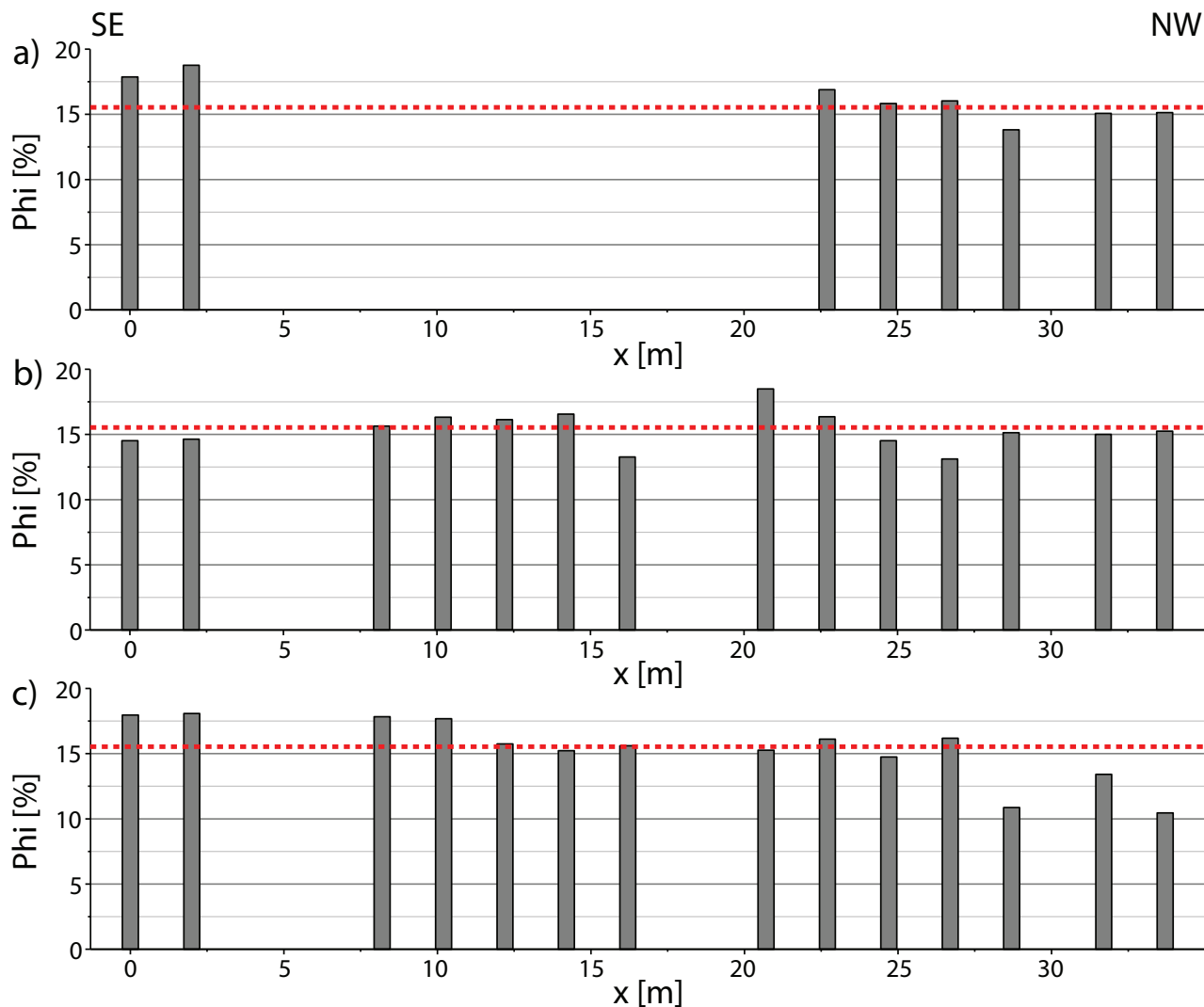
Fig. 7: Spectral gamma ray curve of profile 1 (samples RB 08 to RB 21) along the quarry wall. The average spectral gamma radiation is at 150.1 API (dashed line) (max. 169.2 API, min. 135.8 API).

Fig. 8: Cross plot of permeability versus porosity with the colour code indicating the position of the specific sample along the quarry wall (numbers   distance from SE to NW in metres).
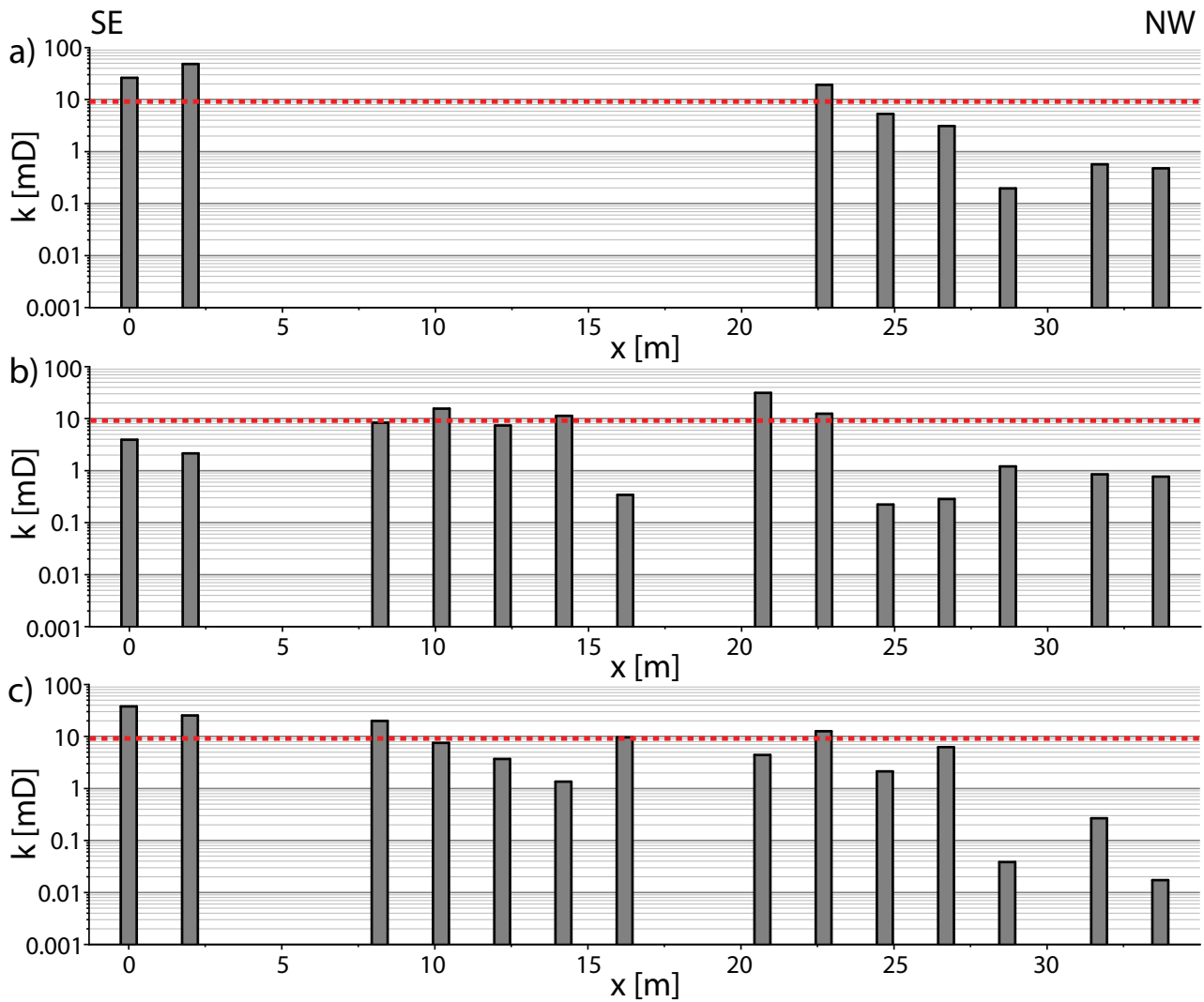
Fig. 9: Porosity profiles along the quarry wall from SE to NW (**a**   upper profile 3, **b**   middle profile 2, **c**   basal profile 1) with the aver age porosity of 15.5 % displayed as dashed line (max. 18.8 %, min. 10.5 %). The average standard deviation accounts for 0.2 %.

5. Discussion

Sedimentology
Very shallow beds gently dipping towards the NW (Fig. 2a: no. 1) along the quarry section ending asymptotically at the basal bounding surface in the upper sandstone bed (Fig. 2a: no. 3) are interpreted as lateral accretion surfaces (Stewart 1981; Miall 1985; Cadle & Cairncross 1993). They illustrate the ongoing migration of a point bar with the cut bank to the NW following the palaeochannel (Heggemann et al. 2003; Bridge 2006). The erosive character of the basal bounding surface of the upper sandstone bed (Fig. 2a: no. 3) is also characteristic for lateral accretion elements (Stewart 1981; Miall 1985, 1988b; Cadle & Cairncross 1993). Its erosive character also prohibits the preservation of a gradational, non-erosive upper bounding surface of the basal sand body,

which is another typical aspect of lateral accretion elements but is known to often be truncated by the subsequent sedimentary unit (Miall 1985; Cadle & Cairncross 1993). First-order bounding surfaces (Fig. 2a: no. 1) outline lenses of a sigmoidal shape typical for lateral accretion features (Marzo et al. 1988). This overall characteristic outline is often obscured by smaller-scale, secondary channels (Miall 1985) as it is the case in the basal unit featuring two m-scale channel geometries (Fig. 2a: no. 2). Downstream accretion on the m-scale is excluded as mechanism forming those surfaces considering their shallow dip and substantial lateral extent along the 35 m wide quarry section (Ghazi & Mountney 2009). Furthermore, the Upper Buntsandstein of the region was formed primarily by deposits of meandering river systems (Geyer 2002; Bock et al. 2005; Okrusch et al. 2011; Freuden-berger et al. 2013). Meanders may also exhibit downstream

Fig. 10: Permeability profiles along the quarry wall from SE to NW (**a** upper profile 3, **b** middle profile 2, **c** basal profile 1) with the average value of 9.19 mD displayed as dashed lines (max. 48.43 mD, min. 0.02 mD).

accretion but lateral accretion is more frequently encountered in a laterally migrating system (Ghazi & Mountney 2009). Another published example of a meander deposit of the Plattensandstein is the quarry Wüstenzell approximately 10 km east of the study area. Quarry Wüstenzell also features fine-grained, red, cross-bedded sandstone bodies of lenticular shape with few intercalated claystone layers (Freudenberger 1990; Bock et al. 2005).
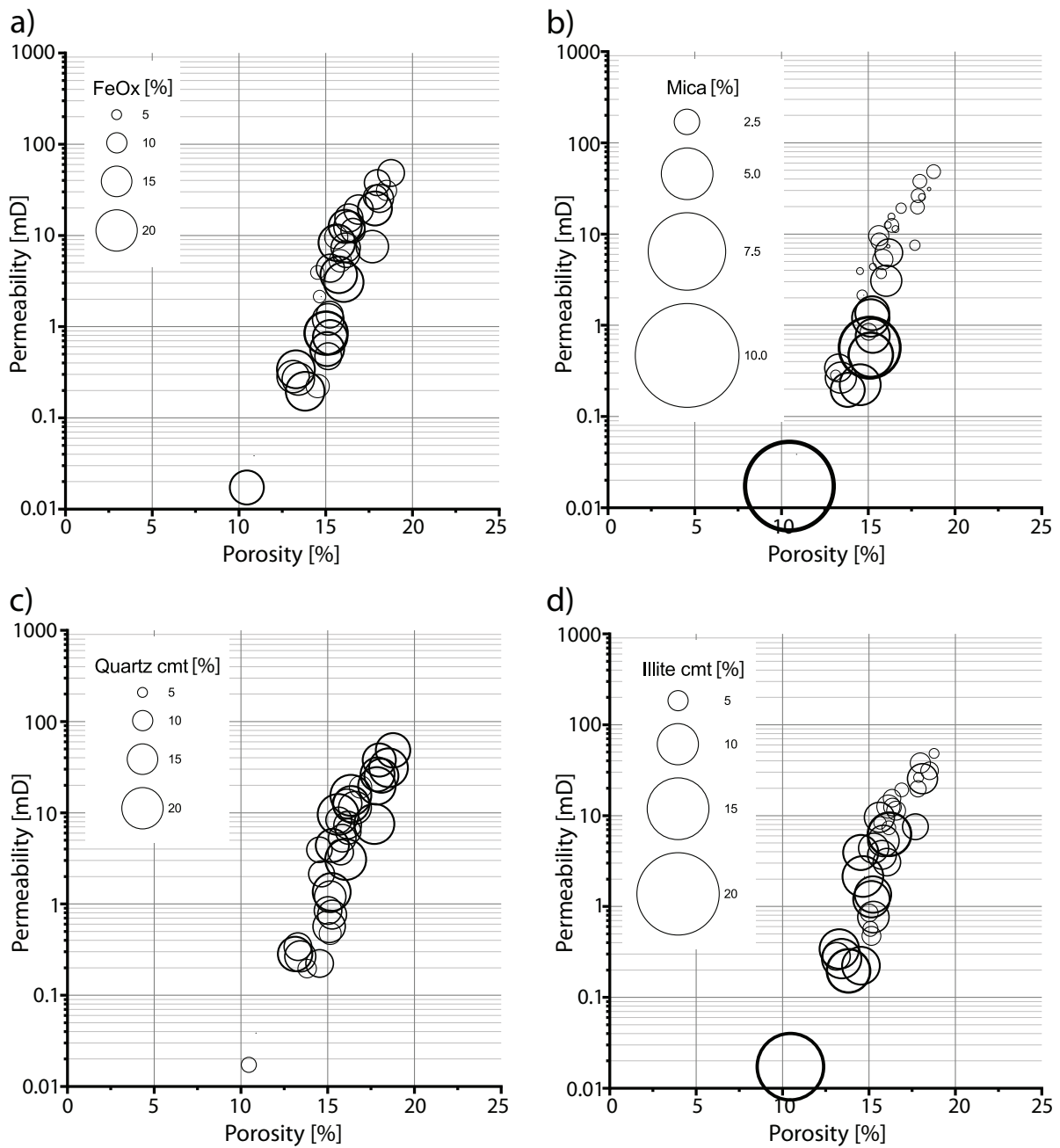
The narrow, shallow channels (2 and 4 m in width) seen in profile in the upper part of the basal bed along the SW-wall (Fig. 2a: no. 2) can be assigned to cross-bar channels in the upper point bar deposit of a fluvial meander. Those are mostly discussed to form through discharge fluctuations and shifts in the channel position (Bridge 2006), or in stages of receding water levels (Sambrook Smith et al. 2016).

The occurrence of subhorizontal bedding at the top of the basal bed along the NW-wall points toward a deposition as either lower or upper plane beds of the corresponding flow regime (Ashley 1990; Fig. 2a: no. 1). The fine to very fine grain size of on average 150 µm indicates upper plane beds according to bedform stability diagrams (Ashley 1990; Van den Berg & Van Gelder 1993; Carling 1999). The upper plane beds (Fig. 2a: no. 1), like the cross-bar channels, are assigned to the top part of a point bar deposit prior to a change in flow velocities or base-level causing the subsequent erosive surface (Bridge 2006; Fig. 2a: no. 3).

The lower and upper sandstone units are separated by an erosive, subhorizontal surface, which may represent a limited base-level fall or increasing energy in the river system causing successive erosion (Fig. 2a: no. 3). Such multi-storey fluvial channels match well with fluvial meanders in a semiarid environment, as described for the wider region (Füchtbauer 1967, 1974; Paul 1982; Tietze 1982; Mader & Teyssen 1985; Bock et al. 2005; Okrusch et al. 2011; Freudenberger et al. 2013; Meschede & Warr 2019).
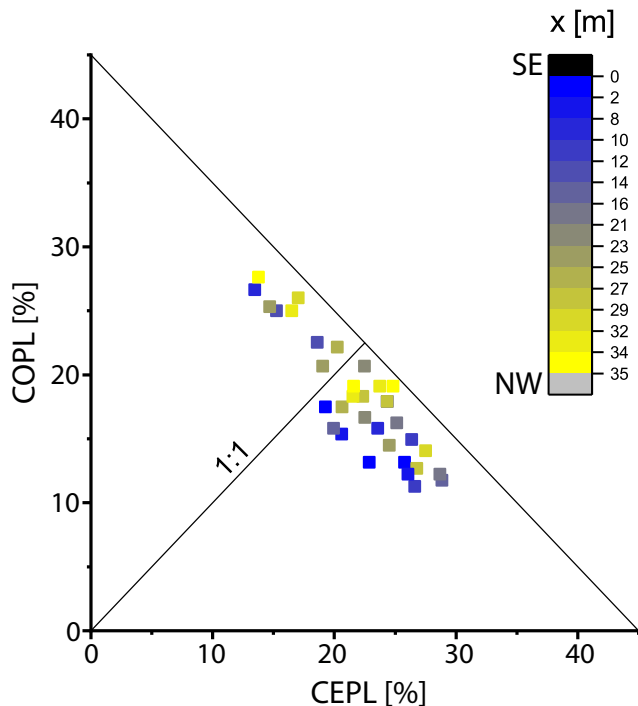
Fig. 11: Bubble chart exhibiting relationships between porosity, permeability, and mineral phases. (**a**) The contents of iron oxide FeOx rich grains poorly correlate with porosity and permeability. (**b**) Samples containing high contents of detrital micas have lower permeability and porosity. (**c**) Quartz cement content shows a poor correlation with porosity and permeability. (**d**) Samples containing higher illite contents have lower porosity and permeability.

In the upper bed of the SE-wall, foresets of higher dip angles, having a tangential character, and reduced lateral extent can be interpreted as downstream accretion surfaces (Ghazi & Mountney 2009; Fig. 2a: no. 1).

The presence of rip-up clasts of silt- and claystones (samples RB-17 and RB-19 in profile 1) near the base of the basal bed indicates that rip-up clasts preferentially occur in the vicinity of the bottomsets of fluvial cosets as also reported in similar settings (Veiga et al. 2002; Komatsubara 2004; Bridge 2006; Henares et al. 2016a). Their angular clast morphology suggests an intraformational origin as reworked clasts from a nearby floodplain (Bordy & Catuneanu 2002; Veiga et al. 2002; Grecula et al. 2003; Heggemann et al. 2003; Komatsubara 2004; Geyer 2005; Bridge 2006; Henares et al. 2016a).

Fig. 12: Plot after Lundegard (1992) with results plotting both in the cementational porosity loss (CEPL) dominated area (25 out of 36 samples) and compactional porosity loss (COPL) dominated area (11 out of 36 samples) (blue SE part of outcrop, yellow NW part of outcrop).

Spectral gamma ray and mineral composition
Overall high SGR values of the Plattensandstein are assigned to a high fraction of fine-grained material and relatively high amounts of micas, illite and K-feldspar (Supplementary Table). The lateral variation of spectral gamma ray values in the study area indicates differences in the sandstone composition related to those minerals as well as rip-up clast or rock fragments (Fig. 7). For the studied quarry walls, the increase of the SGR-signal is well reflected by the increase of detrital mica contents towards the NW in petrographic samples (Fig. 5b). Micas are reported to be abundant in fluvial deposits and cause higher SGR values (North & Boering 1999). Their content has been proven to occasionally be higher in floodplain deposits when compared to channel sandstones, thus SGR-signals may be characteristic for floodplain and channel. Signals may also overlap for those two facies obscuring an increase in mica content toward the floodplain (North & Boering 1999). A decrease in flow velocities favouring the deposition of sheet silicates within the channel may explain the increase of detrital mica to the NW. This hypothesis is supported by the sedimentological structures: Surfaces interpreted as lateral accretion (Fig. 2a: no. 1) illustrate a progressive channel migration with assumed increasing curvature of the meandering channel prior to its eventual abandonment. Increasing curvature coincides with reduced current energy of the river (Chang 1983; Blanckaert & de Vriend 2010) and

thus possibly increased mica deposition. As the overall sedimentary texture does not change, it can be assumed that such velocity reduction is small.

Centimetre-scale rip-up clasts presumably originating from a nearby floodplain occur more frequently in the NW-part of the studied quarry. Thus, an increased gamma ray signal related to detrital mica content and including the presence of clayey to silty rip-up clasts might indicate an increase in eroded intraformational sediments.
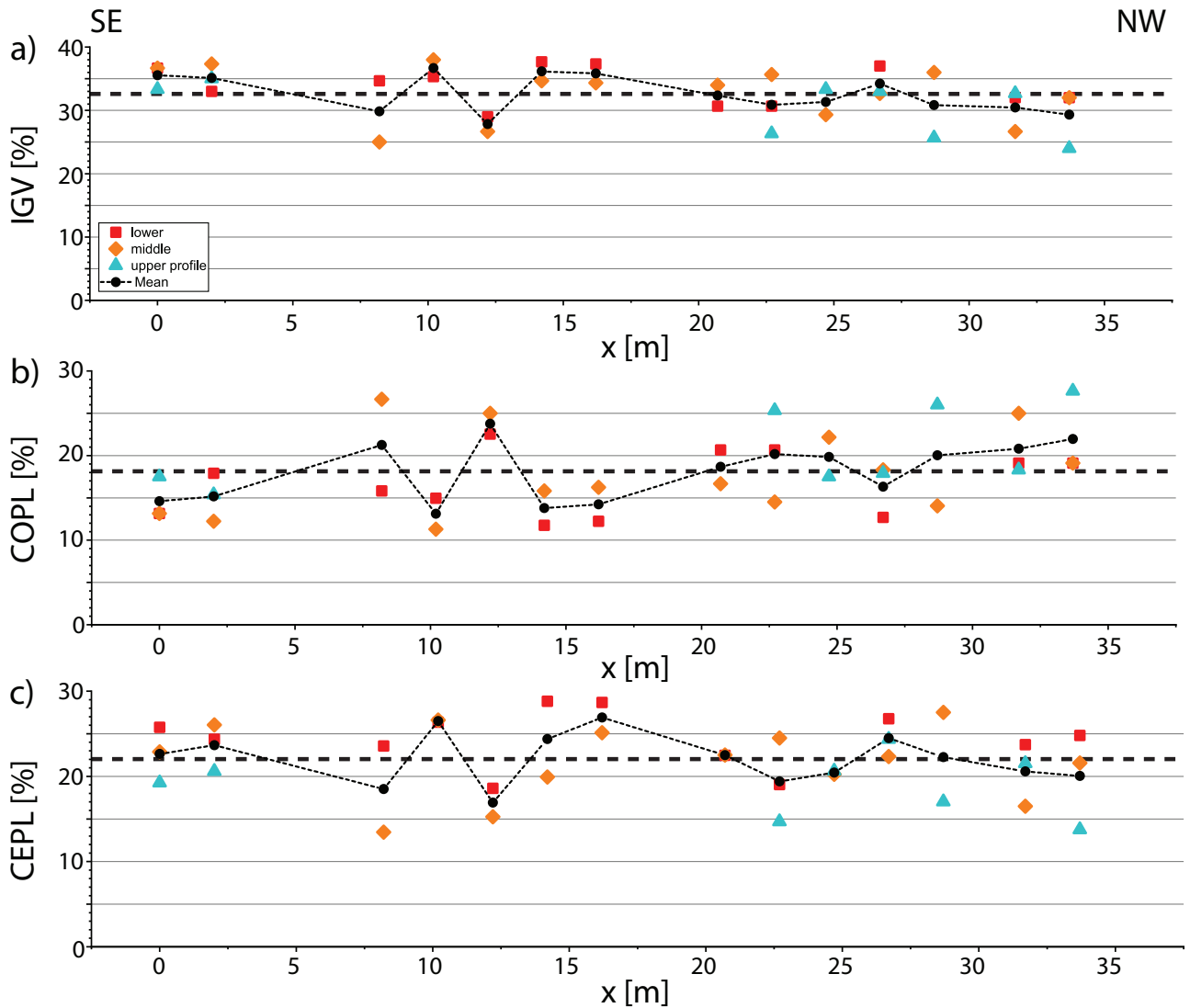
Paragenetic sequence
Based on the textural observations for authigenic cements (Figs. 4d–h) and comparison with published data, a relative paragenetic sequence can be established (Fig. 14).

The earliest diagenetic alteration is interpreted to be the infiltration of grain coating clay minerals and sediment reddening by pigmented hematite rims (Walker 1967a, 1967b, 1975; Walker et al. 1978; Morad et al. 2010; Beyer et al. 2014; Busch et al. 2017). They frequently occur at grain contacts and are overgrown by all other authigenic phases (Figs. 4d, f, g).

An early diagenetic feldspar (and rock fragment) dissolution enables the subsequent formation of feldspar cements. Those euhedral feldspar cements are interpreted to grow during early diagenesis in arid depositional environments (Füchtbauer 1974; Morad et al. 2010; Okkerman & Gaupp 2011; Beyer et al. 2014; Beyer 2015) and are partially encased by subhedral quartz overgrowths (Fig. 4d). Consequently, feldspar cements are interpreted to predate quartz cementation. The observation of quartz cement filling a fracture in a euhedral feldspar overgrowth further supports this interpretation, which is in accordance with results of other authors for the Buntsandstein in Central Germany (Füchtbauer 1967, 1974).

For dolomite an early diagenetic formation is described in literature (Worden & Burley 2003; Worden et al. 2018). Based on textural relationships and the replacement of feldspar cements in the presented samples, this can be interpreted for parts of the studied dolomite cements. The pore-filling cement texture, which appears to stabilize the grain framework, prevents long grain contacts, and encloses detrital grains (Fig. 4e, left). From this observation an early diagenetic origin is interpreted. It is supported by the fact that no early or burial diagenetic, syntaxial cement phase like feldspar and quartz are observed underneath the pore-filling dolomite. A burial diagenetic or uplift related formation of dolomite rhombs (Fig. 4e, top) is interpreted, where quartz and feldspar cements are enclosed or replaced by those rhombs, thus postdating both cement phases. The pitted appearance of both dolomite cement textures is interpreted to be a result of uplift-related dissolution by meteoric waters (Fig. 4e; Al-Ramadan et al. 2005; Bjørlykke 2014). Staining did not reveal compositional differences between the observed dolomite cements.

The dissolution of K-feldspar grains, and their replacement by illite and alteration to kaolinite could be assigned to different processes (Fig. 4g; Weber & Lepper 2002). The formation of kaolinite is favoured during early diagenetic weath-

Fig. 13: Scatter plots along the quarry wall for all profiles (dashed line average value, dotted line mean of the three samples at position x). (**a**) The intergranular volume IGV (avg. 33 %, max. 38 %, min. 24 %). (**b**) Porosity loss by compaction (avg. 18 %, max. 28 %, min. 11 %). (**c**) Porosity loss by cementation (avg. 22 %, max. 29 %, min. 13 %) of all samples along the profiles.

ering of feldspar grains when in contact with meteoric waters (Füchtbauer 1974; Lanson et al. 2002; Worden & Morad 2003; Morad et al. 2010; Bjørlykke 2014; Becker et al. 2017). The stability of kaolinite is largely related to kinetic constraints and the K$^+$/H$^+$ activity ratio during diagenesis (Lanson et al. 2002; Lander & Bonnell 2010). Pore-filling kaolinite occurrence is low in the presented samples, which can be assigned to pervasive subsequent illitisation with available K$^+$ from feldspar dissolution or from external sources at low acidity (Lanson et al. 2002; Busch et al. 2020). Thus a sufficient supply of K$^+$ is implied as well as high precipitation rates at 120–140 °C with precipitation starting already at lower temperatures during burial (Bjørlykke 1998). Additionally, arid conditions at early burial may have also slowed kaolinite formation during early diagenesis, as observed in fluvial sandstones in an arid environment during the Upper Car-

boniferous (Becker et al. 2017, 2019). The replacement of feldspars by illite occurs prominently along the twin planes (Molenaar et al. 2015; Busch et al. 2019). Illitisation of feldspars is interpreted as a burial diagenetic alteration.

The illitisation of infiltrated, likely smectitic and hematite-stained clay mineral grain coatings is interpreted to follow the early diagenetic phase of K-feldspar dissolution and kaolinite formation, supplying the K$^+$-ions. The illitisation also likely predates quartz cementation since illitised coatings are overgrown by syntaxial quartz cements (Fig. 4d). A burial diagenetic replacement of smectitic precursor clays is also reported for other sandstones deposited in arid depositional systems (Liewig & Clauer 2000). The replacing reactions of kaolinite and illite after feldspar and kaolinite respectively produce minor amounts of excess silica, which could source the formation of quartz cements (Weber & Lep-

Fig. 14: Paragenetic sequence of the study area.

per 2002; Morad et al. 2010; Beyer et al. 2014). Illitised parts of feldspar grains remain as a meshwork within intragranular pores (Fig. 4g).
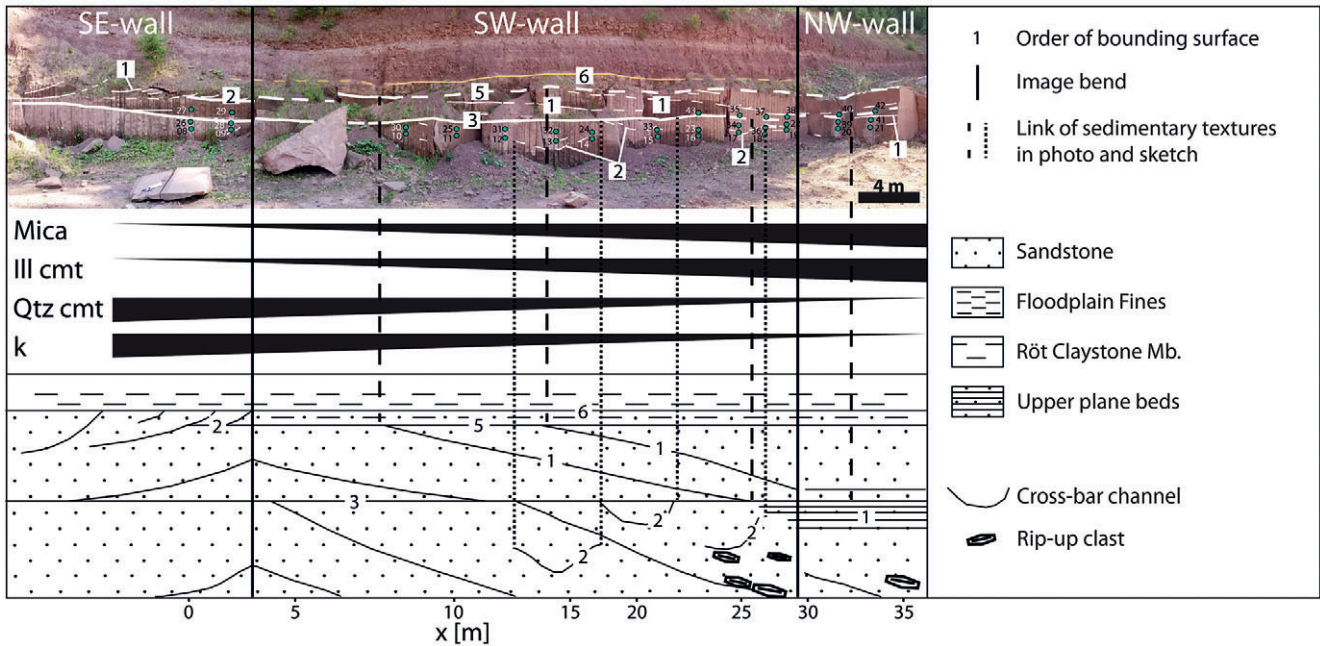
Quartz cementation likely syn- to postdates mechanical and chemical compaction, since samples containing a compacted fabric contain visually less quartz cements (Figs. 4a, b) than less compacted samples (Fig. 4d). Sources for quartz cements could be intraformational pressure dissolution resulting in serrated grain contacts (Fig. 4b; Walderhaug & Bjørkum 2003), clay mineral transformations or feldspar replacements and dissolution (Lander & Walderhaug 1999; Worden & Morad 2003; Morad et al. 2010). Quartz cementation is generally described to be a burial diagenetic alteration, being pervasive at temperatures above 70–75 °C (Walderhaug 1996, 2000; Lander & Walderhaug 1999; Morad et al. 2010; Taylor et al. 2010) and kinetically controlled if the pore fluid is near the saturation with SiO_2 (Rimstidt & Barnes 1980; Walderhaug 1996).

Quartz cements are absent in some intragranular pores in feldspars that were partially replaced by illite and maintaining the original grain outlines (Fig. 4g). This dissolution is interpreted to postdate syntaxial quartz cementation and illitisation. It likely coincides with uplift diagenetic dissolution of unstable detrital grains and partial dissolution of dolomite cements when flushed by meteoric fluids (Becker et al. 2017; Wüstefeld et al. 2017; Fig. 4e).

The formation of minor amounts of TiOx cements is often related to the dissolution and alteration of Ti-bearing detrital mineral grains (e.g. ilmenite, sphene or biotite; Füchtbauer 1974; Morad & Aldahan 1986, 1987; Sindern et al. 2019). Anatase dating in Permian Rotliegend sandstones from the NW-German Basin, deposited in an arid depositional environment by Sindern et al. (2019) support a timing prior to illite precipitation but state that both illite and TiOx formed during the initial stages of burial diagenesis. Generally, the diagenetic formation of pore-filling titanium oxide aggregates is known to occur as an early to burial diagenetic phase (Morad & Aldahan 1986, 1987). As the few titanium oxide aggregates in the samples do not appear strongly affected by compaction a burial diagenetic formation is interpreted. As aggregates occur surrounded by quartz cement, they are interpreted to predate or coincide with the formation

Fig. 15: Composite image showing sedimentary structures in the panoramic photo and the sedimentological sketch. Black triangles display the lateral distribution of rock properties influencing reservoir quality (triangular bars indicating increases and decreases in mica, illite and quartz content as well as permeability k).

of authigenic quartz supporting an early burial diagenetic formation (Figs. 4h, 14).

Minor amounts of chlorite replacements of rock fragments and micas do not show a distinct paragenesis with other minerals, but are reported to be prominent burial diagenetic replacements of ferromagnesian-rich grains (as e.g. volcanic rock fragments or biotite; Anjos et al. 2003; Worden & Morad 2003).

The bleaching of thin laminae within the sandstones, discolouring the originally red sandstone to a whitish colour is interpreted to be due to the alteration of grain rimming iron oxide phases (Chan et al. 2000; Beitler et al. 2003; Hilse et al. 2010). The alteration is interpreted to postdate the first dolomite cementation preserving substantial iron oxide rims (Fig. 4e). The timing of bleaching is interpreted to coincide with early diagenetic feldspar cementation and the initial stages of quartz cementation since bleached areas do still exhibit minor iron oxide pigments on grain outlines overgrown by syntaxial, blocky feldspar- and quartz cements (Fig. 4d; Schmidt et al. 2020).

Reservoir quality controls
Sandstone permeability varies over almost four orders of magnitude (0.02 to 48.43 mD) over distances of 33.7 m laterally and 1.2 m vertically in this study (Figs. 10, 12). Permeability variations in other fluvial deposits are reported to also extend over three orders of magnitude, due to sedimentary structures, lithological variability and compaction of ductile rock fragments (Wachutka & Aigner 2001; Hartkamp-Bakker & Donselaar 2009; McKinley et al. 2011; Becker et al.

2017). The observed permeability decrease toward the NW-part of the profiles can be related to compositional differences (Figs. 5, 6, 11). While rocks contain slightly higher mean iron oxide FeOx grain contents to the NW (Fig. 5a), Fig. 11a illustrates that the amount of iron oxide FeOx grains is not linked to porosity or permeability. For feldspar cements the scatter plot (Fig. 6c) displays that cement quantity is not directly related to the measured porosity or permeability. The mean mica content of all profiles increases from 24.7 m onwards as the permeabilities show below-average values (Figs. 5b, 10). The detrital mica content is negatively correlated with porosity and permeability (Fig. 11b). This can be explained by micas being prone to mechanical compaction and enhancing chemical compaction (pressure dissolution) of detrital quartz grains (Bjørkum et al. 1993; Elghali et al. 2006; Greene et al. 2009; Morad et al. 2010; Kristiansen et al. 2011; Henares et al. 2016b; Becker et al. 2017). Similarly, increased contents of authigenic illite filling the pore space promote pressure dissolution of quartz at grain contacts (Fig. 4h). This can be related to reduced permeability (Figs. 6b, 10, 11d) towards the NW-part, which is in accordance to other outcrop analog and subsurface studies (Gaupp et al. 1993; Worden & Morad 2003; Morad et al. 2010; Bjørlykke 2014; Monsees et al. 2020). No clear correlation can be established for quartz cements and reservoir quality (Fig. 11c). Samples in the NW with highest mica (Fig. 5b) and illite contents (Fig. 6b) exhibit larger COPL-values (Fig. 13b) related to enhanced chemical compaction prior to quartz cementation (Greene et al. 2009; Kristiansen et al. 2011; Beyer et al. 2014; Monsees et al. 2020).

Mica contents (Fig. 5b) increasing toward the NW and the occurrence of rip-up clasts in the NW may suggest more intraformational erosion and re-deposition of such clasts and dispersed clayey material from a floodplain (Fig. 15). This results in increasing API-values towards the NW (Fig. 7) and is reflected by an increasing mean of COPL-values due to chemical compaction (Fig. 13b; Henares et al. 2016b). From sedimentary structures it is interpreted that channel migration in this meandering system (e.g. Bock et al. 2005; Okrusch et al. 2011; Freudenberger et al. 2013) took place toward the NW (Figs. 2, 15). The palaeochannel centres of the basal and the upper sandstone unit are expected to lie further to the NW prior to abandonment (Fig. 15). Thus, the illite contents increasing to the NW may originate from increased infiltration of precursory, detrital clay near the floodplain or from the proximity of an overlying, abandoned palaeochannel (Moraes & Surdam 1993). The deposition of micas (Fig. 5b, profile 3) and clay particles, which during burial diagenesis undergo illitisation to the NW can be related to an overall decreasing flow velocity of the river system with lateral accretion and increasing channel curvature.

The outcrop is representative for the Plattensandstein of the region and results may be applicable to explain reservoir quality variations on a regional scale. Similar sampling at equivalent outcrops in the wider study area could support the findings of this study.

6. Conclusion

The outcrop exposes a Lower Triassic multi-storey fluvial meander with point bar deposits and cross-bar channels. The two fine-grained sandstone beds are separated by an erosive surface and feature lateral accretion surfaces.

The variation in porosity (10.5 to 18.8 %, avg. 15.5 %) ranges over 8 % and permeability (0.02 to 48.43 mD, avg. 9.19 mD) ranges over three orders of magnitude over 35 m laterally and 1.2 m vertically in the fine-grained sandstones.

The lateral decrease of permeabilities to the NW is reflected in all three profiles and can be related to an increased content of detrital mica and authigenic illite. Furthermore, the lateral variation of mica and illite is well reflected in spectral gamma ray signatures with an increase of 19 API from the average value.

The increased amount of detrital mica to the NW of the study area enhances chemical compaction and reduces available intergranular pore space and permeability. The amount of illite may add to chemical compaction and porosity reduction.

7. Acknowledgements

8. References

Aigner, T. & Bachmann, G.H. (1992): Sequence stratigraphic framework of the German Triassic. Sediment. Geol., 80: 115 135.

Al Ramadan, K., Morad, S., Proust, J.N. & Al Aasm, I. (2005): Distribution of diagenetic alterations in siliciclastic shoreface deposits within a sequence stratigraphic framework: Evidence from the Upper Jurassic, Boulonnais, NW France. J. Sediment. Res., 75 (5): 943 959; https://doi.org/10.2110/jsr.2005.072.

Anjos, S.M.C., De Ros, L.F. & Silva, C.M.A. (2003): Chlorite authigenesis and porosity preservation in the Upper Cretaceous marine sandstones of the Santos Basin, offshore eastern Brazil. In: Worden, R.H. & Morad, S. (ed.): Clay mineral cements in sandstones: 291 316; Oxford (Blackwell).

Ashley, G.M. (1990): Classification of large scale subaqueous bed forms: A new look at an old problem. J. Sediment. Petrol., 60 (1): 160 172.

Backhaus, E. (1974): Limnische und fluviatile Sedimentation im südwestdeutschen Buntsandstein. Geol. Rundsch., 63 (3): 925 942; https://doi.org/10.1007/BF01821318.

Backhaus, E. (1981): Der marin brackische Einfluß im Oberen Röt Süddeutschlands. Z. Dt. Geol. Ges., 132 (1): 361 382.

Becker, I., Wüstefeld, P., Koehrer, B., Felder, M. & Hilgers, C. (2017): Porosity and permeability variations in a tight gas sand stone reservoir analogue, Westphalian D, Lower Saxony Basin, NW Germany: Influence of depositional setting and diagenesis. J. Pet. Geol., 40: 363 389; https://doi.org/10.1111/jpg.12685.

Becker, I., Busch, B., Koehrer, B., Adelmann, D. & Hilgers, C. (2019): Reservoir quality evolution of Upper Carboniferous (Westphalian) tight gas sandstones, Lower Saxony Basin, NW Germany. J. Pet. Geol., 42: 371 392; https://doi.org/10.1111/jpg.12742.

Beitler, B., Chan, M.A. & Parry, W.T. (2003): Bleaching of Jurassic Navajo Sandstone on Colorado Plateau Laramide highs: Evi dence of exhumed hydrocarbon supergiants? Geology, 31 (12): 1041 1044; https://doi.org/10.1130/G19794.1.

Bertier, P., Swennen, R., Lagrou, D., Laenen, B. & Kemps, R. (2008): Palaeo climate controlled diagenesis of the Westphal ian C & D fluvial sandstones in the Campine Basin (north east Belgium). Sedimentology, 55 (5): 1375 1417; https://doi.org/10.1111/j.1365 3091.2008.00950.x.

Beyer, D. (2015): Evolution of reservoir properties in the Lower Triassic aquifer sandstones of the Thuringian Syncline in Cen tral Germany. Doctoral thesis, Univ. Jena: 124 p.

Beyer, D., Kunkel, C., Aehnelt, M., Pudlo, D., Voigt, T., Nover, G. & Gaupp, R. (2014): Influence of depositional environment and diagenesis on petrophysical properties of clastic sediments (Buntsandstein of the Thuringian Syncline, Central Germany). Z. Dt. Ges. Geowiss., 165 (3): 345 365; https://doi.org/10.1127/1860 1804/2014/0072.

Bjørkum, P.A., Walderhaug, O. & Aase, N.E. (1993): A model for the effect of illitization on porosity and quartz cementation of sandstones. J. Sediment. Petrol., 63: 1089 1091.

Bjørlykke, K. (1998): Clay mineral diagenesis in sedimentary ba sins A key to the prediction of rock properties. Examples from the North Sea Basin. Clay Miner., 33 (1): 15 34; https://doi.org/10.1180/000985598545390.

Bjørlykke, K. (2014): Relationships between depositional environ ments, burial history and rock properties. Some principal as pects of diagenetic process in sedimentary basins. Sediment. Geol., 301: 1 14; https://doi.org/10.1016/j.sedgeo.2013.12.002.

Blanckaert, K. & de Vriend, H.J. (2010): Meander dynamics: A nonlinear model without curvature restrictions for flow in open channel bends. J. Geophys. Res., 115 (F4): F04011; https://doi.org/10.1029/2009JF001301.

Bock, H., Freudenberger, W., Lepper, J., Schmitt, P. & Weber, J. (2005): Der Buntsandstein in Main Tauberfranken (Exkursion B am 31. März 2005). Jber. Mitt. Oberrhein. Geol. Ver., 87: 65 96; https://doi.org/10.1127/jmogv/87/2005/65.

Böse, M., Ehlers, J. & Lehmkuhl, F. (2018): Deutschlands Norden: 201 p.; Berlin (Springer); https://doi.org/10.1007/978 3 662 55373 2.

Bordy, E.M. & Catuneanu, O. (2002): Sedimentology of the Beau fort Molteno Karoo fluvial strata in the Tuli Basin, South Af rica. South African J. Geol., 105: 51 66.

Bridge, J.S. (2006): Fluvial facies models: Recent developments. In: Posamentier, H.W. & Walker, R.G. (ed.): Facies models revisited. Soc. Econ. Paleontol. Mineral., Spec. Publ., 84: 85 170.

Busch, B., Hilgers, C., Gronen, L. & Adelmann, D. (2017): Cemen tation and structural diagenesis of fluvio aeolian Rotliegend sandstones, northern England. J. Geol. Soc. London, 174: 855 868; https://doi.org/10.1144/jgs2016 122.

Busch, B., Hilgers, C., Lander, R.H., Bonnell, L.M. & Adelmann, D. (2018): Reservoir quality and burial model evaluation by kinetic quartz and illite cementation modeling: Case study of Rotliegendes, north Germany. AAPG Bull., 102 (2): 293 307; https://doi.org/10.1306/0503171605217075.

Busch, B., Becker, I., Koehrer, B., Adelmann, D. & Hilgers, C. (2019): Porosity evolution of two Upper Carboniferous tight gas fluvial sandstone reservoirs: Impact of fractures and total cement volumes on reservoir quality. Mar. Pet. Geol., 100: 376 390; https://doi.org/10.1016/j.marpetgeo.2018.10.051.

Busch, B., Hilgers, C. & Adelmann, D. (2020): Reservoir quality controls on Rotliegend fluvio aeolian wells in Germany and the Netherlands, Southern Permian Basin Impact of grain coat ings and cements. Mar. Pet. Geol., 112: 104075; https://doi.org/10.1016/j.marpetgeo.2019.104075.

Cadle, A.B. & Cairncross, B. (1993): A sandy, bed load dominated fluvial system deposited by lateral accretion: Permian Karoo Sequence, South Africa. Sediment. Geol., 85: 435 455.

Canham, A.C., Love, M.A., Racey, A. & Polachan, S. (1996): Stra tigraphy and reservoir potential of the Mesozoic Khorat Group, NE Thailand. J. Pet. Geol., 19 (3): 321 338.

Carling, P.A. (1999): Subaqueous gravel dunes. J. Sediment. Res., 69 (3): 534 545; https://doi.org/10.2110/jsr.69.534.

Chan, M.A., Parry, W.T. & Bowman, J.R. (2000): Diagenetic hema tite and manganese oxides and fault related fluid flow in Juras sic sandstones, Southeastern Utah. AAPG Bull., 84: 1281 1310.

Chang, H.H. (1983): Energy expenditure in curved open channels. J. Hydraulic Eng., 109 (7): 1012 1022.

Deutsche Stratigraphische Kommission (ed.; Koordination und Ge staltung: Menning, M. & Hendrich, A.) (2016): Stratigraphi sche Tabelle von Deutschland 2016; Potsdam (GeoForschungs Zentrum).

Dickson, J.A.D. (1966): Carbonate identification and genesis as re vealed by staining. J. Sediment. Petrol., 36 (2): 491 505.

Doyle, J.D. & Sweet, M.L. (1995): Three dimensional distribution of lithofacies, bounding surfaces, porosity, and permeability in a fluvial sandstone Gypsy Sandstone of Northern Oklahoma. AAPG Bull., 79: 70 96.

El ghali, M.A.K., Mansurbeg, H., Morad, S., Al Aasm, I. & Ajdan lisky, G. (2006): Distribution of diagenetic alterations in fluvial and paralic deposits within sequence stratigraphic framework: Evidence from the Petrohan Terrigenous Group and the Svidol Formation, Lower Triassic, NW Bulgaria. Sediment. Geol., 190 (1/4): 299 321; https://doi.org/10.1016/j.sedgeo.2006. 05. 021.

Fischer, C., Dunkl, I., Von Eynatten, H., Wijbrans, J.R. & Gaupp, R. (2012): Products and timing of diagenetic processes in Upper Rotliegend sandstones from Bebertal (North German Basin, Parchim Formation, Flechtingen High, Germany). Geol. Mag., 149 (5): 827 840; https://doi.org/10.1017/S001675681 1001087.

Folk, R.L. (1980): Petrology of sedimentary rocks: 182 p.; Austin (Hemphill Publ.).

Folk, R.L. & Ward, W.C. (1957): Brazos river bar: A study in the significance of grain size parameters. J. Sediment. Petrol., 27 (1): 3 26.

Frank, M. (1937): Ergebnisse neuer Untersuchungen über Fazies und Bildung von Trias und Jura in Südwest Deutschland. Geol. Rundsch., 28: 465 498.

Freudenberger, W. (1990): Erläuterungen zu Blatt 6223 Wertheim; Stuttgart (Landesvermessungsamt Baden Württemberg).

Freudenberger, W., Geyer, G. & Schröder, B. (2013): Der Bunt sandstein im nördlichen Bayern (nordwestliches Franken, Bruchschollenland und Randfazies im Untergrund. In: Lep per, J., Röhling, H. G. & Subkommission Perm Trias der DSK (ed.): Stratigraphie von Deutschland, XI. Buntsandstein. Schriftenr. Dt. Ges. Geowiss., 69: 547 582.

Füchtbauer, H. (1967): Der Einfluss des Ablagerungsmilieus auf die Sandsteindiagenese im Mittleren Buntsandstein. Sedi ment. Geol., 1: 159 179.

Füchtbauer, H. (1974): Zur Diagenese fluviatiler Sandsteine. Geol. Rundsch., 63 (3): 904 925; https://doi.org/10.1007/ BF01821317.

Füchtbauer, H. (1988): Sedimente und Sedimentgesteine; 4th ed.: 1141 p.; Stuttgart (Schweizerbart).

Gaupp, R., Matter, A., Platt, J., Ramseyer, K. & Walzebuck, J. (1993): Diagenesis and fluid evolution of deeply buried Per mian (Rotliegende) gas reservoirs, Northwest Germany. AAPG Bull., 77: 1111 1128.

Geyer, G. (2002): Geologie von Unterfranken und angrenzenden Regionen: 588 p., Gotha (Klett Perthes).

Geyer, G. (2005): The Fish River Subgroup in Namibia: Stratigra phy, depositional environments and the Proterozoic Cambrian boundary problem revisited. Geol. Mag., 142 (5): 465 498; https://doi.org/10.1017/S0016756805000956.

Geyer, O.F., Gwinner, M.P., Geyer, M., Nitsch, E., Simon, T. & Ellwanger, D. (2011): Geologie von Baden Württemberg; 5th ed.: 627 p.; Stuttgart (Schweizerbart).

Ghazi, S. & Mountney, N.P. (2009): Facies and architectural ele ment analysis of a meandering fluvial succession: The Permian Warchha Sandstone, Salt Range, Pakistan. Sediment. Geol., 221 (1/4): 99 126; https://doi.org/10.1016/j.sedgeo.2009.08. 002.

Grecula, M., Flint, S.S., Wickens, H.D.V. & Johnson, S.D. (2003): Upward thickening patterns and lateral continuity of Permian sand rich turbidite channel fills, Laingsburg Karoo, South Af rica: Topographically controlled channel overbank system. Sedimentology, 50 (5): 831 853; https://doi.org/10.1046j.1365 3091.2003.00576.x.

Greene, G.W., Kristiansen, K., Meyer, E.E., Boles, J.R. & Is raelachvili, J.N. (2009): Role of electrochemical reactions in pressure solution. Geochim. Cosmochim. Acta, 73 (10): 2862 2874; https://doi.org/10.1016/j.gca.2009.02.012.

Hagdorn, H., Nitsch, E., Aigner, T. & Simon, T. (2009): Field guide. In: International Triassic Field Workshop, Triassic of South west Germany, September 7 11, 2009, Tübingen and Ingelfin gen: 72 p.; http://www.stratigraphie.de/perm trias/trias work shops.html.

Hartkamp Bakker, C.A. & Donselaar, M.E. (2009): Permeability patterns in point bar deposits: Tertiary Loranca Basin, central Spain. In: Bryant, I.D. & Flint, S.S.(ed.): The geological mod elling of hydrocarbon reservoirs and outcrop analogues: 157 168; Chichester (Wiley).

Heald, M.T. & Larese, R.E. (1974): Influence of coatings on quartz cementation. J. Sediment. Petrol., 44 (4): 1269 1274.

Heggemann, H., Tietze, K. W. & Behr, H. J. (2003): The river sys tem of the Phra Wihan Formation, Thailand. Göttinger Arb. Geol. Paläont., 5: 23 32.

Henares, S., Arribas, J., Cultrone, G. & Viseras, C. (2016a): Muddy and dolomitic rip up clasts in Triassic fluvial sandstones: Ori gin and impact on potential reservoir properties (Argana Basin, Morocco). Sediment. Geol., 339: 218 233; https://doi. org/10.1016/j.sedgeo.2016.03.020.

Henares, S., Caracciolo, L., Viseras, C., Fernández, J. & Yeste, L.M. (2016b): Diagenetic constraints on heterogeneous reser voir quality assessment: A Triassic outcrop analog of meander ing fluvial reservoirs. AAPG Bull., 100 (9): 1377 1398.

Hilse, U., Goepel, A., Pudlo, D., Heide, K. & Gaupp, R. (2010): Characterization of CO_2 induced (?) bleaching phenomena in German red bed sediments by combined geochemical and evolved gas analysis. Geophys. Res. Abstr., 12: 1684 1685.

Howarth, R.J. (1998): Improved estimators of uncertainty in pro portions, point counting, and pass fail test results. Am. J. Sci., 298: 594 607.

Hurst, A. & Nadeau, P.H. (1995): Clay microporosity in reservoir sandstones: An application of quantitative electron microscopy in petrophysical evaluation. AAPG Bull., 79: 563 573.

Kirchner, H. (1927): Über die Tierfährten im oberen Buntsandstein. Paläont. Z., 9: 112 121.

Klinkenberg, L.J. (1941): The permeability of porous media to liq uids and gases. Drill. Prod. Pract., API 41 200; New York (American Petroleum Inst.).

Komatsubara, J. (2004): Fluvial architecture and sequence stratig raphy of the Eocene to Oligocene Iwaki Formation, northeast Japan: Channel fills related to the sea level change. Sedi ment. Geol., 168 (1/2): 109 123; https://doi.org/10.1016/j. sedgeo.2004.03.005.

Kristiansen, K., Valtiner, M., Greene, G.W., Boles, J.R. & Israelach vili, J.N. (2011): Pressure solution The importance of the electrochemical surface potentials. Geochim. Cosmochim. Acta, 75 (22): 6882 6892; https://doi.org/10.1016/j.gca.2011. 09.019.

Lander, R.H. & Bonnell, L.M. (2010): A model for fibrous illite nucleation and growth in sandstones. AAPG Bull., 94 (8): 1161 1187; https://doi.org/10.1306/04211009121.

Lander, R.H. & Walderhaug, O. (1999): Predicting porosity through simulating sandstone compaction and quartz cementation. AAPG Bull., 83 (3): 433 449.

Lander, R.H., Larese, R.E. & Bonnell, L.M. (2008): Toward more accurate quartz cement models: The importance of euhedral versus noneuhedral growth rates. AAPG Bull., 92 (11): 1537 1563; https://doi.org/10.1306/07160808037.

Lanson, B., Beaufort, D., Berger, G., Bauer, A., Cassagnabère, A. & Meunier, A. (2002): Authigenic kaolin and illitic minerals dur ing burial diagenesis of sandstones: A review. Clay Miner., 37 (1): 1 22; https://doi.org/10.1180/0009855023710014.

Liewig, N. & Clauer, N. (2000): K Ar dating of varied microtex tural illite in Permian gas reservoirs, northern Germany. Clay Miner., 35 (1): 271 281; https://doi.org/10.1180/0009855005 46648.

Line, L.H., Jahren, J. & Hellevang, H. (2018): Mechanical compac tion in chlorite coated sandstone reservoirs Examples from Middle Late Triassic channels in the southwestern Barents Sea. Mar. Pet. Geol., 96: 348 370; https://doi.org/10.1016/j. marpetgeo.2018.05.025.

Lü, Z. X., Ye, S. J., Yang, X., Li, R. & Qing, Y. H. (2015): Quanti fication and timing of porosity evolution in tight sand gas reser voirs: An example from the Middle Jurassic Shaximiao Forma tion, western Sichuan, China. Petroleum Sci., 12 (2): 207 217; https://doi.org/10.1007/s12182 015 0021 1.

Lundegard, P.D. (1992): Sandstone porosity loss A 'big picture' view of the importance of compaction. J. Sediment. Petrol., 62 (2): 250 260.

Mader, D. & Teyssen, T. (1985): Palaeoenvironmental interpreta tion of fluvial red beds by statistical analysis of paleocurrent data: Examples from the Buntsandstein (Lower Triassic) of the Eifel and Bavaria in the German Basin (Middle Europe). Sed iment. Geol., 41: 1 74.

Martini, E. (1992): Fossilien, Sedimentmarken und Palökologie im Oberen Buntsandstein (Röt) der Rhön. Natur u. Museum, 122: 90 99.

Marzo, M., Nijman, W. & Puigdefabregas, C. (1988): Architecture of the Castissent fluvial sheet sandstones, Eocene, South Pyre nees, Spain. Sedimentology, 35: 719 738.

McKinley, J.M., Atkinson, P.M., Lloyd, C.D., Ruffell, A.H., Worden, R.H. (2011): How porosity and permeability vary spa tially with grain size, sorting, cement volume, and mineral dis solution in fluvial Triassic sandstones: The value of geostatis tics and local regression. J. Sediment. Res., 81: 844 858; ht tps://doi.org/10.2110/jsr.2011.71.

Menning, M. (2018): Die Stratigraphische Tabelle von Deutschland 2016 (STD 2016) / The Stratigraphic Table of Germany 2016 (STG 2016). Z. Dt. Ges. Geowiss., 169 (2): 105 128.

Meschede, M. & Warr, L.N. (2019): The geology of Germany A process oriented approach: 304 p.; Cham (Springer Nature).

Miall, A.D. (1977): Lithofacies types and vertical profile models in braided river deposits: A summary. In: Miall, A.D. (ed.): Flu vial sedimentology. Can. Soc. Pet. Geol., Mem.: 597 604.

Miall, A.D. (1985): Architectural element analysis: A new method of facies analysis applied to fluvial deposits. Earth Sci. Rev., 22: 261 308.

Miall, A.D. (1988a): Architectural elements and bounding surfaces in fluvial deposits: Anatomy of the Kayenta Formation (Lower Jurassic), Southwest Colorado. Sediment. Geol., 55: 233 262.

Miall, A.D. (1988b): Reservoir heterogeneities in fluvial sand stones: Lessons from outcrop studies. AAPG Bull., 72: 682 697.

Miall, A.D. (1996): The geology of fluvial deposits: Sedimentary facies, basin analysis, and petroleum geology: 582 p.; Berlin (Springer).

Miall, A.D. (2014): The facies and architecture of fluvial systems. In: Miall, A. (ed.): Fluvial depositional systems: 25 35; Cham (Springer); https://doi.org/10.1007/978 3 319 00666 6.

Miall, A.D. & Turner Peterson, C.E. (1989): Variations in fluvial style in the Westwater Canyon Member, Morrison Formation (Jurassic), San Juan Basin, Colorado Plateau. Sediment. Geol., 63: 21 60.

Molenaar, N., Felder, M., Bär, K. & Götz, A.E. (2015): What classic greywacke (litharenite) can reveal about feldspar diagenesis: An example from Permian Rotliegend sandstone in Hessen, Germany. – Sediment. Geol., 326: 79–93; https://doi.org/10.1016/j.sedgeo.2015.07.002.

Monsees, A.C., Busch, B., Schöner, N. & Hilgers, C. (2020): Rock typing of diagenetically induced heterogeneities – A case study from a deeply buried clastic Rotliegend reservoir of the Northern German Basin. – Mar. Pet. Geol., 113: 104163; https://doi.org/10.1016/j.marpetgeo.2019.104163.

Morad, S. & Aldahan, A.A. (1986): Alteration of detrital Fe-Ti oxides in sedimentary rocks. – Geol. Soc. Am., Bull., 97: 567–578.

Morad, S. & Aldahan, A.A. (1987): Diagenetic "replacement" of feldspars by titanium oxides in sandstones. – Sediment. Geol., 51: 147–153.

Morad, S., Al-Ramadan, K., Ketzer, J.M. & De Ros, L.F. (2010): The impact of diagenesis on the heterogeneity of sandstone reservoirs: A review of the role of depositional facies and sequence stratigraphy. – AAPG Bull., 94: 1267–1309; https://doi.org/10.1306/04211009178.

Moraes, M.A.S. & Surdam, R.C. (1993): Diagenetic heterogeneity and reservoir quality: Fluvial, deltaic, and turbiditic sandstone reservoirs, Potiguar and Reconcavo rift basins, Brazil. – AAPG Bull., 77: 1142–1158; https://doi.org/10.1306/BDFF8E20-1718-11D7-8645000102C1865D.

North, C.P. & Boering, M. (1999): Spectral gamma ray logging for facies discrimination in mixed fluvial-eolian successions: A cautionary tale. – AAPG Bull, 83: 155–169.

Okkerman, J.A. & Gaupp, R. (2011): Diagenesis and reservoir quality of Rotliegend sandstones in the Northern Netherlands, a review. – In: Grötsch, J. (ed.): The Permian Rotliegend of the Netherlands: 193–226; Tulsa (SEPM).

Okrusch, M., Geyer, G., Lorenz, J., Jung, J. & Matthes, S. (2011): Spessart: Geologische Entwicklung und Struktur, Gesteine und Minerale. – Sammlung geologischer Führer, 106: 368 p.; Stuttgart (Borntraeger).

Paul, J. (1982): Der Untere Buntsandstein des Germanischen Beckens. – Geol. Rundsch., 71 (3): 795–811; https://doi.org/10.1007/BF01821104.

Paxton, S.T., Szabo, J.O., Ajdukiewicz, J.M. & Klimentidis, R.E. (2002): Construction of an intergranular volume compaction curve for evaluating and predicting compaction and porosity loss in rigid-grain sandstone reservoirs. – AAPG Bull., 86 (12): 2047–2067.

Pranter, M.J., Ellison, A.I., Cole, R.D. & Patterson, P.E. (2007): Analysis and modeling of intermediate-scale reservoir heterogeneity based on a fluvial point-bar outcrop analog, Williams Fork Formation, Piceance Basin, Colorado. – AAPG Bull., 91 (7): 1025–1051; https://doi.org/10.1306/02010706102.

Rider, M.H. & Kennedy, M. (2011): The geological interpretation of well logs; 3rd ed.: 440 p.; Sutherland (Rider-French).

Rieckmann, M. (1970): Untersuchung von Turbulenzerscheinungen beim Fließen von Gasen durch Speichergesteine unter Berücksichtigung der Gleitströmung. – Erdoel Erdgas Z., 86: 36–51.

Rimstidt, J.D. & Barnes, H.L. (1980): The kinetics of silica-water reactions. – Geochim. Cosmochim. Acta, 44: 1683–1699.

Röhling, H.-G. & Lepper, J. (2013): Paläogeographie des Mitteleuropäischen Beckens während der tieferen Trias (Buntsandstein). – In: Lepper, J., Röhling, H.-G. & Subkommission Perm-Trias der DSK (ed.): Stratigraphie von Deutschland, XI. Buntsandstein. – Schriftenr. Dt. Ges. Geowiss., 69: 43–67.

Röhling, H.-G., Lepper, J., Diehl, M., Dittrich, D., Freudenberger, W., Friedlein, V., Hug-Diegel, N. & Nitsch, E. (2018): Der Buntsandstein in der Stratigraphischen Tabelle von Deutschland 2016 / The Buntsandstein Group in the Stratigraphic Table of Germany 2016. – Z. Dt. Ges. Geowiss., 169 (2): 151–180; https://doi.org/10.1127/zdgg/2018/0132.

Sambrook Smith, G.H., Best, J.L., Leroy, J.Z. & Orfeo, O. (2016): The alluvial architecture of a suspended sediment dominated meandering river: The Río Bermejo, Argentina. – Sedimentology, 63 (5): 1187–1208; https://doi.org/10.1111/sed.12256.

Scherer, M. (1987): Parameters influencing porosity in sandstones: A model for sandstone porosity prediction. – AAPG Bull., 71 (5): 485–491.

Schmidt, C., Busch, B. & Hilgers, C. (2020): Compaction and cementation control on bleaching in Triassic fluvial red beds, S-Germany. – Z. Dt. Ges. Geowiss, 172 (1): ••• – ••• [this volume]; https://doi.org/10.1127/zdgg/2020/0233.

Schröder, B. (1982): Entwicklung des Sedimentbeckens und Stratigraphie der klassischen Germanischen Trias. – Geol. Rundsch., 71 (3): 783–794; https://doi.org/10.1007/BF01821103.

Schultz-Krutisch, T. & Heller, F. (1985): Measurement of magnetic susceptibility anisotropy in Buntsandstein deposits from southern Germany. – J. Geophys., 56: 51–58.

Sindern, S., Havenith, V., Gerdes, A., Meyer, F.M., Adelmann, D. & Hellmann, A. (2019): Dating of anatase-forming diagenetic reactions in Rotliegend sandstones of the North German Basin. – Int. J. Earth Sci., 108 (4): 1275–1292; https://doi.org/10.1007/s00531-019-01705-x.

Stewart, D.J. (1981): A meander-belt sandstone of the Lower Cretaceous of Southern England. – Sedimentology, 28: 1–20.

Taylor, A.W. & Ritts, B.D. (2004): Mesoscale heterogeneity of fluvial-lacustrine reservoir analogues: Examples from the Eocene Green River and Colton Formations, Uinta Basin, Utah, USA. – J. Pet. Geol., 27 (1): 3–26.

Taylor, T.R., Giles, M.R., Hathon, L.A., Diggs, T.N., Braunsdorf, N.R., Birbiglia, G.V., Kittridge, M.G., Macaulay, C.I. & Espejo, I.S. (2010): Sandstone diagenesis and reservoir quality prediction: Models, myths, and reality. – AAPG Bull., 94 (8): 1093–1132; https://doi.org/10.1306/04211009123.

Tietze, K.-W. (1982): Zur Geometrie einiger Flüsse im Mittleren Buntsandstein (Trias). – Geol. Rundsch., 71 (3): 813–828.

Trendell, A.M., Atchley, S.C. & Nordt, L.C. (2012): Depositional and diagenetic controls on reservoir attributes within a fluvial outcrop analog: Upper Triassic Sonsela member of the Chinle Formation, Petrified Forest National Park, Arizona. – AAPG Bull., 96 (4): 679–707; https://doi.org/10.1306/08101111025.

Trusheim, F. (1937): Wurzelböden im Plattensandstein Mainfrankens. – Zbl. Mineral., Geol. Paläontol., B 10: 385–388.

Tyler, N. & Finley, R.J. (1991): Architectural controls on the recovery of hydrocarbons from sandstone reservoirs. – In: Miall, A.D. & Tyler, N. (ed.): The three-dimensional facies architecture of terrigenous clastic sediments, and its implications for hydrocarbon discovery and recovery. – Concepts Sedimentol. Paleontol., 3: 1–5.

Udden, J.A. (1914): Mechanical composition of clastic sediments. – Geol. Soc. Am., Bull., 25 (1): 655–744.

Van den Berg, J.H. & Van Gelder, A. (1993): A new bedform stability diagram, with emphasis on the transition of ripples to plane bed in flows over fine sand and silt. – In: Marzo, M. & Puigdefábregas, C. (ed.): Alluvial sedimentation: 11–21; Oxford (Blackwell).

Veiga, G.D., Spalletti, L.A. & Flint, S. (2002): Aeolian/fluvial interactions and high-resolution sequence stratigraphy of a non-

marine lowstand wedge: The Avilé Member of the Agrio Formation (Lower Cretaceous), central Neuquén Basin, Argentina. Sedimentology, 49: 1001 1019.

Wachutka, M. & Aigner, T. (2001): Reservoirgeologie und Petrophysik: Eine Aufschluss Analogstudie im Buntsandstein (Trias, Schwarzwald, SW Deutschland). Z. Angew. Geol., 47: 191 198.

Walderhaug, O. (1996): Kinetic modeling of quartz cementation and porosity loss in deeply buried sandstone reservoirs. AAPG Bull., 80: 731 745.

Walderhaug, O. (2000): Modeling quartz cementation and porosity in Middle Jurassic Brent Group Sandstones of the Kvitebjørn Field, Northern North Sea. AAPG Bull., 84: 1325 1339.

Walderhaug, O. & Bjørkum, P.A. (2003): The effect of stylolite spacing on quartz cementation in the Lower Jurassic Sto Formation, Southern Barents Sea. J. Sediment. Res., 73: 146 156; https://doi.org/10.1306/090502730146.

Walker, T.R. (1967a): Color of recent sediments in tropical Mexico: A contribution to the origin of red beds. Geol. Soc. Am., Bull., 78: 917 920.

Walker, T.R. (1967b): Formation of red beds in modern and ancient deserts. Geol. Soc. Am., Bull., 78: 353 368.

Walker, T.R. (1975): Red beds in the western interior of the United States. In: Paleotectonic investigations of the Pennsylvanian System in the United States: 49 56; Washington (U.S. Government Print. Office).

Walker, T.R., Waugh, B. & Grone, A.J. (1978): Diagenesis in first cycle desert alluvium of Cenozoic age, southwestern United States and northwestern Mexico. Geol. Soc. Am., Bull., 89: 19 32.

Weber, J. & Lepper, J. (2002): Depositional environment and diagenesis as controlling factors for petrophysical properties and weathering resistance of siliciclastic dimension stones: Integrative case study on the "Wesersandstein" (northern Germany, Middle Buntsandstein). In: Siegesmund, S., Weiss, T.N. & Vollbrecht, A.: Natural stone, weathering phenomena, conser

vation strategies and case studies; 205th ed.: 103 114; London (Geol. Soc. London).

Wentworth, C.K. (1922): A scale of grade and class terms for clastic sediments. J. Geol., 30 (5): 377 392.

Wilson, J.C. & McBride, E.F. (1988): Compaction and porosity evolution of Pliocene sandstones, Ventura Basin, California. AAPG Bull., 72: 664 681.

Worden, R.H. & Burley, S.D. (2003): Sandstone diagenesis: The evolution of sand to stone. In: Burley, S.D. & Worden, R.H. (ed.): Sandstone diagenesis: Recent and ancient: 3 44; Malden (Blackwell).

Worden, R.H. & Morad, S. (ed.) (2003): Clay mineral cements in sandstones: 520 p.; Malden (Blackwell).

Worden, R.H., Armitage, P.J. & Butcher, A.R. (2018): Petroleum reservoir quality prediction: Overview and contrasting approaches from sandstone and carbonate communities. In: Churchill, J.M., Csoma, A.E., Hollis, C., Lander, R.H. & Omma, J.E. (ed.): Reservoir quality of clastic and carbonate rocks: Analysis, modelling and prediction: 1 31; London (Geol. Soc. London).

Wüstefeld, P., Hilse, U., Koehrer, B., Adelmann, D. & Hilgers, C. (2017): Critical evaluation of an Upper Carboniferous tight gas sandstone reservoir analog: Diagenesis and petrophysical aspects. Mar. Pet. Geol., 86: 689 710; https://doi.org/10.1016/j.marpetgeo.2017.05.034.

Ziegler, P.A. (1982): Triassic rifts and facies patterns in Western and Central Europe. Geol. Rundsch., 71 (3): 747 772; https://doi.org/10.1007/BF01821101.

Ziegler, P.A. (1990): Geological atlas of Western and Central Europe; The Hague (Shell Int. Pet. Mij.).

Supplementary Table: All petrographic and petrophysical data as well as calculated parameters for the state of compaction.

Please save the electronic supplement contained in this pdf-file by clicking the blue frame above. After saving rename the file extension to .zip (for security reasons Adobe does not allow to embed .exe, .zip, .rar etc. files).